Dalton
Transactions

PERSPECTIVE

Cite this: *Dalton Trans.*, 2022, **51**, 10320

The impact of secondary coordination sphere engineering on water oxidation reactivity catalysed by molecular ruthenium complexes: a next-generation approach to develop advanced catalysts

Ayyan Ghosh, Sreeja Dasgupta, Animesh Kundu and Sukanta Mandal*

Water oxidation is the bottleneck for producing hydrogen from the water-splitting reaction. Developing efficient water oxidation catalysts (WOCs) has recently been of paramount interest. Ruthenium-based WOCs have gained much attention due to their enriched redox property, robust nature, and superior catalytic performances compared to other transition metal-based molecular catalysts. The performance of a catalyst is highly dependent on the design of the ligand framework. In nature, the secondary coordination sphere around the active site of a metalloenzyme plays a vital role in catalysis. This principle has been employed in the recent development of efficient catalysts. With the aid of secondary interactions, some landmark Ru-based WOCs, producing remarkable turnover frequencies (TOFs) in the order of 10^4 s^{-1}, have been developed. In this account, we have discussed the underlying chemistry related to the effect of secondary interactions (such as hydrogen-bonding, π–π stacking, electrostatic interaction, hydrophobic–hydrophilic environment, *etc.*) on the kinetics of the water oxidation reaction catalysed by molecular Ru-complexes. The use of secondary interactions (such as π–π and C–H⋯π) in anchoring the molecular catalyst onto the solid conducting surface has also been discussed. We aim to provide a brief overview of the positive impact of outer-sphere engineering on water oxidation reactivity, which may offer guidelines for developing the next generation of advanced catalysts.

Received 11th April 2022,
Accepted 30th May 2022

DOI: 10.1039/d2dt01124g

rsc.li/dalton

Department of Chemistry, Indian Institute of Technology Kharagpur, Kharagpur-721302, India. E-mail: sukanta.mandal@chem.iitkgp.ac.in

1. Introduction

The discovery of fire was an essential breakthrough for human civilization. Since then, mankind has had the idea of burning

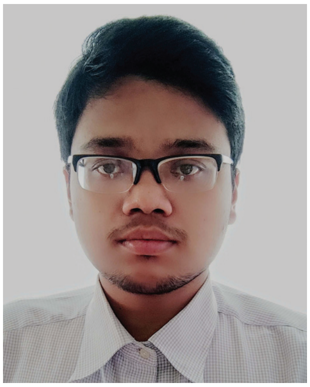

Ayyan Ghosh

Ayyan Ghosh received his B.Sc. degree in Chemistry (Hons.) from the University of Burdwan in 2019. He completed his M.Sc. in Chemistry in 2021 from IIT Kharagpur, where he performed his master's project under the supervision of Dr Sukanta Mandal. Currently, he is a junior research fellow at IIT Kharagpur in Dr Sukanta Mandal's research group. His research focuses on developing molecular complexes with designed ligands for efficient water oxidation catalysis.

Sreeja Dasgupta

Sreeja Dasgupta received her B.Sc. degree in Chemistry (Hons.) in 2018 and subsequently obtained her M.Sc. degree with a specialization in Inorganic Chemistry in 2020 from Jadavpur University, Kolkata. After that, she joined Dr Sukanta Mandal's research group at IIT Kharagpur to pursue her Ph.D. Her research focuses on developing molecular complexes with designed ligands for efficient water oxidation catalysis.

substances to make use of their stored chemical energies. In the modern world, fossil fuels are burnt to utilize their latent energies in the form of electrical energy, mechanical energy and others. But the continuous burning of carbon-rich fossil fuels causes a severe effect on the environment. Burning of biofuels generates toxic substances such as SO_x, NO_x, CO_2, *etc.*, which pollute the environment and contribute to the greenhouse effect. Industrialization scaled up production and, consequently, pollution too. Our living style and societal status have been improved and modernized immensely; however, on the other hand, nature has also been distressed proportionately. The continuous emissions of greenhouse gases into the atmosphere lead to a progressive increase in the average temperature on the Earth's surface. Global warming modifies the weather balances and alters the Earth's climate system, worsening various natural catastrophes including heatwaves, storms, floods and droughts. A recent study has shown an increasing trend in fossil-fuel consumption worldwide to satisfy the energy requirements.[1] Such a huge demand for fossil fuels is crafting an alarming situation all over the world. Scientists have already warned the world's political leaders about the consequences. As a remedial measure, the Paris agreement was signed, where nations negotiated to restrict the burning of fossil fuels to resist the hostile impact of the global warming phenomenon.[2]

Finding an environmentally friendly and sustainable energy source (mainly carbon-free) is urgently required to reduce the dependence on fossil fuels. In this context, renewable energy resources, such as water, wind, tides, sunlight, *etc.*, might play an important role. As per a report, even in this century, only a small percentage (~11%) of the global energy is produced from renewable resources.[1] Such a negligible adoption of renewable resources means most of the investment and research should be devoted to improving the science and technologies to effectively utilise the natural renewable energy sources. Solar energy holds immense potential among natural resources. Sunlight is generally unlimited on the planet; however, its proper utilization is very much limited. Commercial photovoltaic solar panels have efficiencies of around 15%–20%.[3] In comparison, photosynthesis has a much higher efficiency of 30% under standard conditions.[4,5] This means a large portion of the solar energy remains unused. Therefore, the current focus should be on developing technologies that can harvest solar energy efficiently and generate solar fuels. One such possibility is photochemical water-splitting to generate hydrogen gas as a green solar fuel. Fig. 1 presents an artificial photosynthetic modular system that consists of a three-component assembly *viz* a photosensitizer (PS), water oxidation catalyst (WOC) and proton reduction catalyst (PRC).[6] In this device, hydrogen fuel can be generated by splitting water in the presence of sunlight.

From an electrochemical viewpoint, the water-splitting reaction can be separated into two half-cell reactions: anodic water oxidation ($2H_2O \rightarrow O_2 + 4H^+ + 4e^-$; $E^\circ_{ox} = -1.23$ V *vs.* NHE at pH = 0) and cathodic proton reduction ($4H^+ + 4e^- \rightarrow 2H_2$; $E^\circ_{red} = 0.0$ V *vs.* NHE at pH = 0). The oxidation of water is an uphill process ($\Delta G^\circ = +113.38$ kcal mol^{-1}), and this is a difficult step from an electrochemical perspective. The Latimer

Animesh Kundu

Dr Animesh Kundu received his B.Sc. degree in Chemistry (Hons.) from the University of Burdwan in 2013. He obtained his M.Sc. degree in 2015 and subsequently completed his Ph. D. under the supervision of Dr Sukanta Mandal in 2021 at IIT Kharagpur. His doctoral research work was focused on the development of mononuclear ruthenium complexes for water oxidation catalysis. In May 2022, he joined Pailan College of Management & Technology, Kolkata as an Assistant Professor in Chemistry.

Sukanta Mandal

Dr Sukanta Mandal received his Ph.D. in Chemistry from IIT Kanpur, India in 2009 under the supervision of Prof. Rabindranath Mukherjee. Then he was a post-doctoral fellow at the Institute of Chemical Research of Catalonia (ICIQ), Spain with Prof. Antoni Llobet (2009–2011) and at Ewha Womans University, South Korea in a joint project with Prof. Antoni Llobet, Prof. Wonwoo Nam and Prof. Shunichi Fukuzumi (2011–2013). After returning to India, he spent about a year at Assam University, Silchar as DST-INSPIRE Faculty. Afterwards, he was appointed as an Assistant Professor at NIT Patna, where he spent a few months before moving to IIT Kharagpur. Since 2015 (to present), he has been holding a permanent position as Assistant Professor in Chemistry at IIT Kharagpur. His research interests include synthetic bioinorganic model chemistry, bioinspired redox catalysis using transition metal complexes, and water splitting reactions using molecular catalysts.

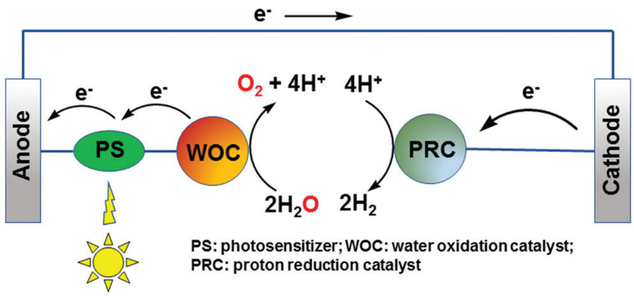

Fig. 1 Schematic representation of the artificial photosynthetic modular system.

diagram for oxygen, depicted in Fig. 2, suggests that water can be oxidised to four different species depending on how many electrons are removed. The thermodynamic barrier for the $1e^-$ or $2e^-$ or $3e^-$ pathway is larger compared to the $4e^-$ process. However, the four-electron process, in contrast, has much more molecular complexity than the other three processes, as it involves the removal of multiple numbers of protons and electrons, and it requires the formation of a kinetically sluggish oxygen–oxygen (O–O) bond.

Photosynthesis is nature's way to harvest and store solar energy in the form of chemical bond energy in foodstuff such as glucose (Calvin cycle).[7] In this whole process, the main hurdle is to overcome the thermodynamic (and kinetic) barrier imposed by the water oxidation step. The oxygen-evolving-complex (OEC) of photosystem (PS) II proficiently catalyses the water oxidation reaction and produces dioxygen in a millisecond timescale. The heart of OEC comprises a $CaMn_4O_5$ cluster. This complex accumulates four oxidation equivalents to accomplish the four-proton and four-electron oxidation of water. Structural elucidation has shown that there are "secondary" amino acid residues around OEC in PS II (Fig. 3) that finely tune the proton relay and reactivity.[8–10] The quantum chemical simulations by Kaila and coworkers on PS II revealed that the electric field generated during the oxidation of redox-active Tyr161 has a significant effect on lowering the energy barrier for the water-mediated proton transfer from the cluster-bound water molecule to the Asp61 residue, leading to the facile generation of the reactive state.[11] Thus, taking a lesson from nature, it can be perceived that the secondary coordination sphere might play an essential role in developing efficient artificial WOCs.

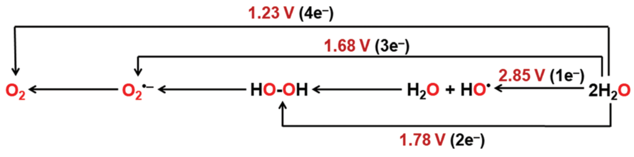

Fig. 2 The Latimer diagram for oxygen. The E°_{red} values are presented *vs.* NHE at pH 0.

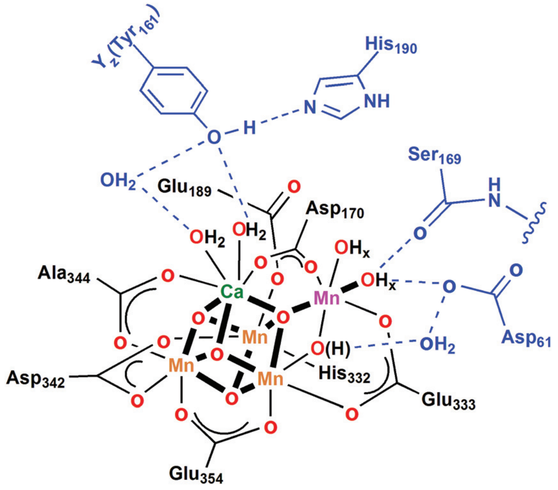

Fig. 3 Schematic representation of the OEC of PS II (PDB 4UB6 and 4UB8) showing the $CaMn_4O_5$ cluster and the hydrogen-bonding network with secondary residues (highlighted with blue colour).

2. Water oxidation reaction: elementary steps

In developing an efficient water oxidation catalyst, it is necessary to understand the mechanistic aspects of the water oxidation steps at the molecular level. To produce one molecule of O_2 from two water molecules, firstly four O–H bonds of the two water molecules need to be activated so that electrons and protons can be removed from them, and afterwards the formation of an O–O bond has to occur. Thus, the designed catalysts that will accomplish the reaction should be capable of removing multiple electrons and protons. In this regard, aquo-ligated metal complexes of the type $[M^{n+}–OH_2]$ are very promising. They can undergo the easy removal of protons and electrons *via* the proton-coupled electron transfer (PCET) pathway to generate high-valent metal–oxo species such as $[M^{(n+2)}{=}O]$. The PCET phenomena with Ru–aquo complexes are well studied in the literature.[12,13] In this way, the hydrogen atoms $(H^+ + e^-)$ from the water molecule can be removed. The PCET process helps to avoid the building-up of Coulombic charges and, thereby, decreases the energy barrier. Once the protons and electrons are removed from water, the next step is to form an oxygen–oxygen bond. This O–O bond formation event is the most crucial step a catalyst should promote effectively. Scheme 1 shows four possible O–O bond formation pathways namely (a) water nucleophilic attack (WNA), (b) interaction of two M–O units (I2M), (c) heterometallic radical coupling pathway (I2M-HC), and (d) oxide relay. The WNA and I2M are very familiar well-established pathways,[6,14] whereas I2M-HC[15,16] and oxide relay[17,18] are non-conventional pathways. The oxide relay and I2M-HC may be considered a subcategory of the WNA and I2M pathways, respectively. In the WNA pathway, a water molecule directly attacks the highly electrophilic oxygen of a metal–oxo unit, forming a [MOOH] hydroperoxo intermediate. On the other hand, in the oxide relay

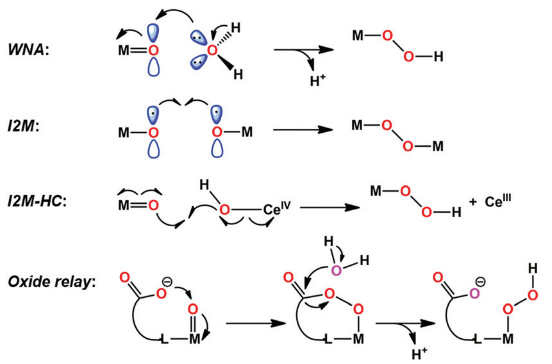

Scheme 1 Different pathways of the O–O bond formation reaction cited in this article.

pathway, a suitably placed dangling oxide nucleophile such as carboxylate might participate in the O–O bond formation reaction intramolecularly to form a putative percarboxylate intermediate that would provide an electrophilic carbon centre for further water nucleophilic attack (Scheme 1).[17,18] In the I2M pathway, two homo metal-oxyl units coupled to each other in a radical coupling pathway to form a [MOOM] peroxo intermediate. Radical coupling might also occur through the heterometallic I2M-HC pathway, particularly in a ceric ammonium nitrate (CAN) driven reaction as shown in Scheme 1.[15,16] The singlet hydroxocerium(IV) ion ($\mathrm{Ce^{IV}}$–OH = $[\mathrm{Ce^{IV}(OH)(NO_3)_5}]^{2-}$) possesses a biradical character ($\mathrm{Ce^{IV}}$–OH ↔ $\mathrm{Ce^{III}}$–$^{\bullet}$OH)[15] that might trigger heterometallic O–O bond formation if the oxo moiety of the metal–oxo unit has a substantial radicaloid character. Therefore, the understanding of the O–O bond formation mechanism is crucial as it opens a door for the structural and electronic tuning of the catalyst to improve the catalytic performances.

3. Primary and secondary interactions

The supporting ligands greatly influence the catalytic performance of a metal complex. In a biological system, the catalytic activity of a metalloenzyme is not only governed by the directly involved coordinating groups at the active site, but the reactivity is also finely controlled by various non-covalent type ancillary interactions.[19] The amino acid residues in a metalloenzyme impose two types of coordination environments around the metal centre. In the first type, a direct interaction (coordination or covalent type) between the metal and ligand donor groups prevails, referred to as primary coordination interactions. In the second type, several non-covalent type (weak) interactions such as hydrogen-bonding, π–π stacking, dipolar, electrostatic, hydrophilic, hydrophobic, steric, *etc.* may succeed due to the pendant residue of the ligands, which do not directly bind with the metal centre, referred to as secondary coordination interactions. It has been realized that a bare active site of a metalloenzyme without the protein surrounding does not perform well. Also, mutations of some amino acid residues in the protein framework leading to destruction or alteration of certain non-covalent interactions may cause a substantial loss in enzyme activity. All these facts infer the essential role of secondary interactions in catalytic performances. The ligands in the primary coordination zone determine the geometry around the metal ion, d-orbital splitting pattern, crystal field stabilization energy, spin state, redox potential, electronic properties, *etc.*, that would certainly influence the energetics of a chemical reaction. Besides those primary effects, the non-covalent interactions in the secondary sphere can exert an additional impact on the energetics, reactivity and selectivity of a reaction by readjusting the chemical and physical properties of the reactive centre as per the requirement of chemical transformations. For instance, the non-covalent interactions can orient the substrates appropriately at the active centre for a selective transformation reaction. Moreover, these weak forces can play vital roles in reducing the kinetic barrier of a reaction by stabilizing the transient intermediates.

As stated above, the water oxidation reaction comprises two crucial steps: (i) removal of protons and electrons, and (ii) formation of an O–O bond, which a catalyst should do proficiently. Secondary interactions can also play a crucial role in assisting these steps. For instance, a hydrogen-bond accepting site in a ligand can activate the hydrogen atoms of the coordinated water by participating in hydrogen-bonding interactions, thus facilitating their removal *via* PCET processes. Similarly, the presence of a pendant base can assist the O–O bond formation *via* the WNA pathway by accepting the protons from the incoming water, which would avoid the generation of higher energetic intermediate such as $[\mathrm{M}^{(n-2)+}\mathrm{OOH_2}]$, thereby reducing the activation barrier of the WNA pathway. Moreover, a pendant base can stabilize various intermediates formed during the water oxidation process by involving hydrogen-bonding interactions, leading to a decrease in the overall kinetic barriers. On the other hand, the presence of auxiliary ligands which can participate in π–π stacking or attractive electrostatic interactions can significantly accelerate the O–O bond formation step between two metal-oxyl units in an I2M pathway. In a $\mathrm{Ce^{IV}}$-driven reaction, the presence of a suitably placed $\mathrm{Ce^{IV}}$–OH capturing group such as sulfonate can appropriately direct the $\mathrm{Ce^{IV}}$–OH unit towards the metal-oxyl to promote the heterometallic O–O bond formation in an I2M-HC pathway. Furthermore, a strategically placed dangling carboxyl group can take part in the O–O bond formation reaction and promote the oxidation of water *via* the oxide relay pathway. Such a process might boost the reaction rate significantly compared to the classical WNA pathway. The pendant oxide nucleophile, residing near the reactive metal–oxo unit, would facilitate O–O bond formation more efficiently over a direct nucleophilic attack from a remote water molecule. Therefore, the design of catalysts interplaying judiciously with secondary coordination sphere interactions would be a promising strategy for developing advanced catalysts in future. In this review article, we have briefly discussed the effect of secondary interactions on the catalytic performances of a few selected molecular Ru-WOCs. We have confined our discussions to only proficient Ru-complexes developed since 2009. The examples are chosen to provide glimpses of various types of secondary interactions which could influence the catalysis.

4. Ruthenium WOCs with pendant functional groups (*e.g.*, sulfonate, carboxylate, phosphonate and pyridyl) in the secondary coordination sphere

4.1. Sulfonate

The design of molecular Ru-WOCs with sulfonate groups in the secondary coordination sphere has drawn much attention recently because of their higher activity, particularly in highly acidic conditions. Although at lower pH water oxidation becomes more challenging, the development of WOCs that can efficiently function at acidic pH is advantageous for the water-splitting reaction since the proton reduction is favoured at acidic pH. Complex **1**, shown in Fig. 4, exhibited high water oxidation activity under acidic conditions.[20] Sulfonate, a stable conjugate base of sulfonic acid ($pK_a < 0$), could remain deprotonated even at low pH and formed strong hydrogen bonds with the coordinated water molecule. The infrared (IR) spectroscopic studies conveyed the weakening of the O–H bond strength of the aquo ligand in **1** due to H-bonding, thus inducing the removal of H-atoms facilely. The computational studies at the density functional level of theory (DFT) revealed that the pendant sulfonate base in **1** assisted the PCET processes *via* intramolecular proton relay even under strongly acidic conditions. All these factors reduced the kinetic barrier, which was reflected in obtaining an impressive electro-catalytic turnover frequency (TOF) at lower pH ($k_{cat} = 1501 \pm 608$ s^{-1} at pH 1.1 and 831 ± 254 s^{-1} at pH 0.43). The water oxidation activity of **1** was also tested in the presence of ceric ammonium nitrate in an acidic medium (pH ~ 1). Interestingly, the sulfonate-bearing complex **1** exhibited higher catalytic performances (TON = 7400 and TOF = 0.88 s^{-1}) as compared to its carboxylic analogue $[Ru(trpy)(HL)(H_2O)]^{2+}$ (trpy: 2,2′:6′,2″-terpyridine; HL = phenanthroline-2-carboxylic acid; TON ~ 700 and TOF = 0.15 s^{-1})[21] under the same Ce^{IV}/pH 1 conditions. The difference in reactivity might be due to the superior proton relay functionality of sulfonate than the carboxylic group at acidic pH (*vide infra*).

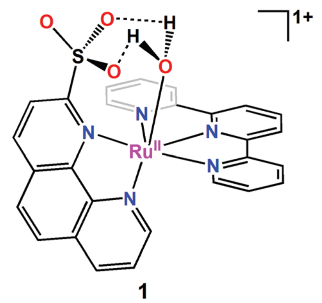

1

Fig. 4 Ruthenium complex having sulfonate as a pendant base (ref. 20).

Besides functioning as a pendant base and facilitating the proton relay process, sulfonate has an affinity binding with strong Lewis-acidic metal ions. The dangling sulfonate group in complex **2** (Fig. 5a) displayed some affinity towards Ce.[22] In support for this fact was the structural characterization of a Ce(III)-sulfonate adduct after reacting **2** with an excess of ceric ammonium nitrate. In complex **2**, one of the two dangling methanesulfonate groups at 5,5′-positions of bipyridine (bpy) is located appropriately to bring together two reactive units Ru^{V}=O and Ce^{IV}–OH in close vicinity for a facile heterometallic O–O bond formation *via* the I2M-HC pathway (Fig. 5b). A proper structure of the possible peroxo intermediate for complex **2** having 5,5′-disubstituted bpy was modelled successfully by computation, as shown in Fig. 5c. Conversely, neither the 4,4′-disubstituted nor the 6,6′-disubstituted derivatives could afford an appropriate computed structure for coupling between Ru–oxo and Ce^{IV}–OH moieties. The effect of the dangling SO_3^- group was manifested by observing a modest two-fold acceleration of the oxygen evolution rate for complex **2** in comparison to the non-substituted complex $[Ru(trpy)(bpy)(OH_2)]^{2+}$. Comparisons of the spectroscopic and electrochemical properties of **2** and $[Ru(trpy)(bpy)(OH_2)]^{2+}$ implied that the pendant SO_3^- group had a negligible influence on the electronic structure of the core complex, establishing the impact of the pendant SO_3^- in the secondary coordination sphere towards rate enhancement.

4.2. Carboxylate

Carboxylate-based ligand frameworks have been used extensively to develop several Ru-WOCs.[6,23] The carboxylate group exerts a very positive impact on both the primary and secondary coordination spheres. The first spectacular demonstration of the secondary coordination sphere effect of carboxylate on catalytic water oxidation reactivity was presented by Llobet's group, who developed complex **3** featuring a [2,2′:6′,2″-terpyridine]-6,6″-dicarboxylate (tda) ligand at the equatorial plane and two pyridine co-ligands at the axial axes (Fig. 6).[24] During the catalytic process, the oxidation state of Ru varied formally

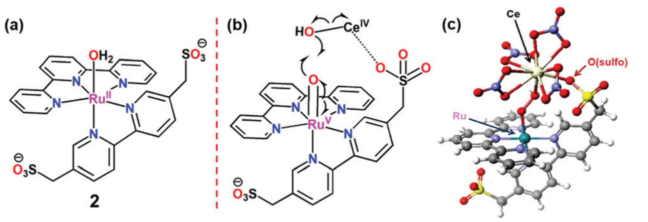

Fig. 5 (a) Ruthenium complex with dangling methanesulfonate groups; (b) schematic representation of the proposed O–O coupling pathway; (c) DFT optimized structure of the possible peroxo intermediate formed *via* coupling between the Ru–oxo moiety and the Ce^{IV}–OH moiety. Figure (c) was adapted with permission from ref. 22. Copyright 2015 John Wiley & Sons, Inc.

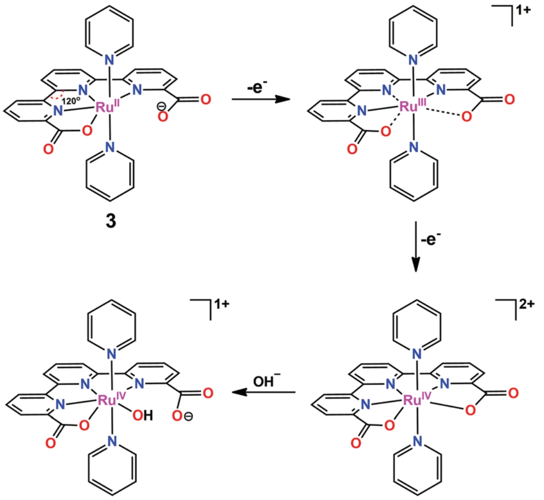

Fig. 6 Drawing of Ru-tda complexes at various oxidation states (ref. 24).

from +II to +V. The single-crystal X-ray diffraction analyses of Ru(II), Ru(III) and Ru(IV) complexes were done. In oxidation state +II, the Ru centre was six-coordinated with an unbound pendant carboxylate. In contrast, at the +IV state, the metal centre expanded its coordination number to seven, forming complex $[Ru^{IV}(tda\text{-}\kappa\text{-}N^3O^2)(py)_2]^{2+}$ (py = pyridine), where all donor atoms of tda were bonded to the Ru centre (Fig. 6). However, in the case of the +III state, the metal centre adopted coordination in-between the coordination number of +II and +IV states (Fig. 6). The strong donor ability of the anionic carboxylate in the primary sphere helped easily access the metal centre at higher oxidation states. The complex $[Ru^{IV}(tda\text{-}\kappa\text{-}N^3O^2)(py)_2]^{2+}$ was apparently catalytically inactive due to a lack of access to aquo ligation. However, during electrolysis under neutral to basic pH conditions, one of the carboxylates at the equatorial site was replaced by an external hydroxide ion to form a catalytically important seven-coordinated $[Ru^{IV}(tda\text{-}\kappa\text{-}N^3O)(OH)(py)_2]^{1+}$ hydroxy species (Fig. 6). This hydroxy species has $pK_a = 5.5$ as determined from the Pourbaix diagram. Thus, at pH > 5.5 the hydroxy species $[Ru^{IV}(tda\text{-}\kappa\text{-}N^3O)(OH)(py)_2]^{1+}$ would be deprotonated to form the formal Ru(IV)–oxo species, $[Ru^{IV}(tda\text{-}\kappa\text{-}N^3O)(O)(py)_2]$, that displayed impressive TOF_{max} values of 8000 s^{-1} at pH 7.0 and 50 000 s^{-1} at pH 10 (determined from the foot of wave analysis, FOWA). The catalytic pathway was proposed based on the electrochemical and DFT calculations, as shown in Fig. 7.[24] Here, the computational studies predicted the indispensable role of the dangling carboxylate that facilitated the proton relay process and stabilized various intermediates by providing the H-bonding site (Fig. 7). These lead to the lowering of activation energies of the rate-determining O–O bond-forming step.

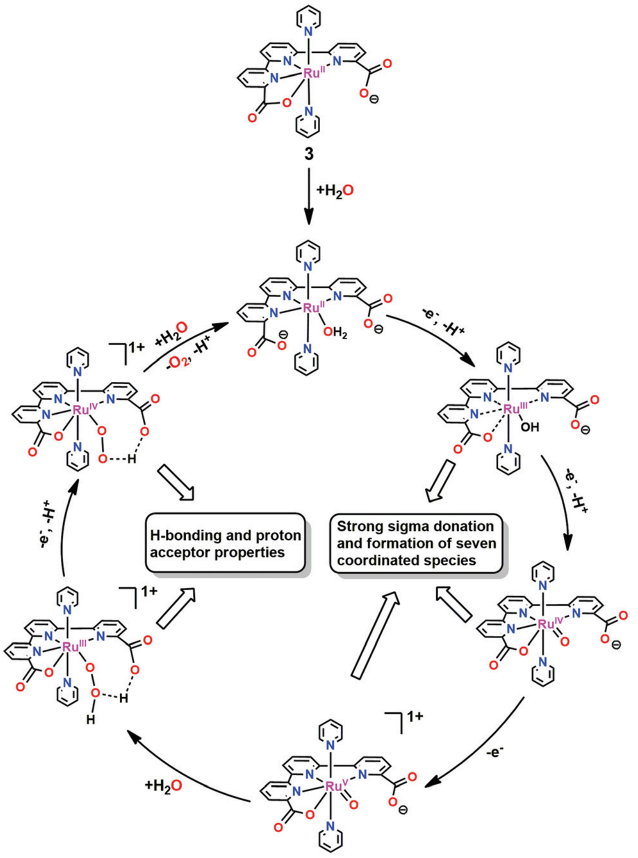

Fig. 7 Proposed water oxidation pathway (based on electrochemical studies and DFT calculations, ref. 24) catalysed by **3** at pH 7.

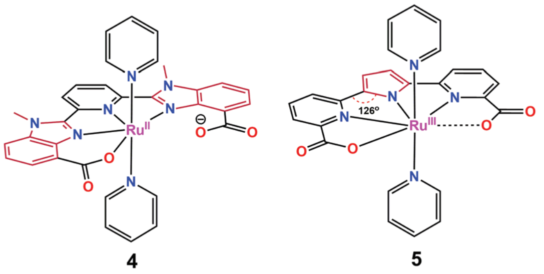

Fig. 8 The Ru-complexes derived *via* modification of the 'tda' ligand framework.

Motivated by the impressive performance of complex **3**, later on various other efficient catalysts were developed utilizing the secondary coordination effect of the carboxylate. Llobet and Akermark groups modified the tda ligand, in which both the terminal pyridyl moieties were replaced by 1-methylbenzimidazoles, to form complex **4** (Fig. 8).[25] In complex **4**, the presence of one extra carbon atom between the coordinating nitrogen and carboxylic group created distortions in the structure due to the formation of a moderately strained six-membered chelate ring. In contrast, in complex **3**, tda formed a stable five-membered ring. Such distortions in **4** weakened the $Ru\text{–}O_{carboxylate}$ bond, allowing easier replacement of the carboxylate by water compared to complex **3**. Expectedly, complex **4** also showed a high catalytic rate, reaching a TOF_{max} of 40 000 s^{-1} at pH 9, comparable to complex **3**. A common mechanistic pathway was proposed for complexes **3** and **4**, where seven-coordinated species were formed at higher oxidation states during the catalytic processes. The expansion of coordination numbers from six to seven positively impacted the water oxidation catalysis. The extra ligation provided the metal centre with an additional electron density that decreased the overpotential to generate the catalytically active high-valent species. Given this beneficial effect of the seven-coordination, a question arises, is it essential for fast catalysis? To address this issue Llobet *et al.* developed another complex **5** modifying the ligand tda, where a pyrrolyl group was inserted by replacing the central pyridyl ring (Fig. 8).[26] The incorporation of the pyrrolyl group introduced two main changes in the coordination properties of the ligand. Firstly, the anionic pyrrolate group provided strong σ-donation to the metal centre. Secondly, the larger $CCN_{pyrrolyl}$ angle (126°), as compared to $CCN_{pyridyl}$ (120°) in tda, increased the constraint of the ligand at the equatorial position by expanding the outer coordination angle at the equatorial plane, which would allow binding of the external aquo ligand to the metal centre; however, at the same time one of the picolinate arms would likely be decoordinated to release the structural strains. DFT calculations predicted the existence of two coordination environments of 6.5 and 6 for the aquated species derived from **5** at the +v oxidation state.[26] These two species, $\mathbf{5^{V}(O)(\kappa\text{-}N^{2.5}O)}$ and $\mathbf{5^{V}(O)(\kappa\text{-}N^{2}O)}$ shown within the second bracket in Fig. 9, differed in energies by only 7.7 kcal mol^{-1}, and thus they could interconvert very quickly in solution. The activation free energies for WNA on 6-coordinated and 6.5-coordinated Ru(v)–oxo species were computed to be 14.2 kcal mol^{-1} and 21.8 kcal mol^{-1}, respectively, at pH 0.0. Therefore, the six-coordinated Ru(v)–oxo species was likely to be the key intermediate that initiated the O–O bond formation reaction *via* the WNA pathway. The anionic pyrrolate group donated a large amount of electron density to the metal centre; consequently, additional seventh coordination was not essential to stabilize the putative +v oxidation state of complex **5**. The aquated Ru(v) species showed excellent activity achieving a TOF$_{max}$ of 9400 s^{-1} at pH 7. Here also, the dangling carboxylate group functioned as an intramolecular proton acceptor as found in the transition state structure computationally, which reduced the activation barrier for the rate-limiting step and ensured fast catalysis. Notably, complex **5** produced the highest TOF$_{max}$ among the three complexes **3**–**5** [8000 s^{-1} (**3**),[24] 1400 s^{-1} (**4**)[25] and 9400 s^{-1} (**5**)[26]] at neutral pH 7. Here, it is to be mentioned that since the basicity of the carboxylate is highly decimated at acidic pH, all these complexes showed promising activities only at neutral to basic conditions.

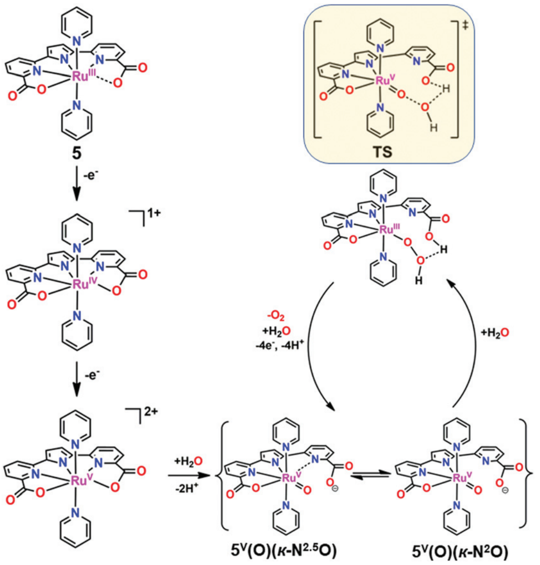

Fig. 9 Schematic representation of intermediates and water oxidation cycle associated with **5**; TS represents the transition state computed for {$\mathbf{5^{V}(O)(\kappa\text{-}N^{2}O)}$ + H_2O} at pH 0.0 (ref. 26).

Besides those functionalities, a suitably placed dangling carboxylate can provide anionic oxygen close to the reactive metal–oxo unit to facilitate the O–O bond formation. Ahlquist *et al.* predicted computationally such an O–O bond formation pathway for complex **3**.[17] The calculations showed that, instead of the typical water nucleophilic attack at the Ru^{V}=O unit, the anionic oxygen of the dangling carboxylate of the tda ligand preferably interacts with Ru^{V}=O to form a putative percarboxylate intermediate that provides an electrophilic carbon centre for further nucleophilic attack from the incoming hydroxide ion, promoting the oxide relay pathway (Fig. 10).[17] The participation of the dangling carboxylate in oxide relay was considered to be the critical factor in achieving such a spectacular catalytic rate for complex **3**. Unfortunately, neither the proton relay (proposed by the Llobet group) nor the oxide relay (proposed by the Ahlquist group) pathways have been experimentally verified for the Ru-tda complex.

In a recent study, our group evaluated the influence of the pendant carboxylic group on the kinetics of the water oxidation reaction by comparing reactivity between two related Ru complexes **6** and **7** (Fig. 11) in an acidic medium.[18] It was found that complex **7** with a pendant carboxylic group showed a significantly higher reaction rate (~21 times) compared to its analogue complex **6** without the dangling carboxylic group (TOF: 0.014 s^{-1} (**6**) and 0.3 s^{-1} (**7**) from the Ce^{IV}-driven reaction; k_{obs}: 0.13 s^{-1} (**6**) and 3 s^{-1} (**7**) from the electrochemical analysis). The isotope labelling experiment using ^{18}O-labelled

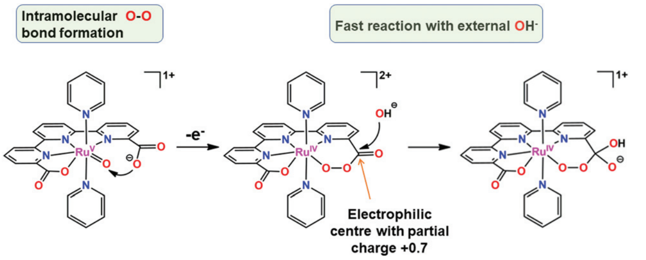

Fig. 10 The unusual oxide relay function of the carboxylate during the catalytic water oxidation reaction by complex **3** at a formal Ru(v) oxidation state from DFT calculations (ref. 17).

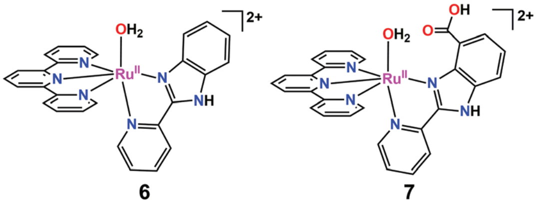

Fig. 11 Two related Ru-complexes with and without the dangling carboxylic group (ref. 18).

water at the Ce(IV)/pH 1/one-turnover condition with complex **7** established the oxide relay pathway instead of the classical WNA. The Ru-compound isolated from the post-catalysis ^{18}O-labelled water was analysed by high-resolution mass spectrometry (HRMS), Fourier transform infrared spectroscopy-attenuated total reflection (FTIR-ATR), and resonance Raman spectroscopy. The data were compared with the sample obtained from the unlabelled water under similar conditions. In HMRS, a two-mass-unit increase in the *m*/*z* value was observed for the labelled sample as compared to the unlabelled sample. In vibrational spectroscopy, an isotopic shift of $\Delta\nu \sim 30$ cm^{-1} in the ν(CO) stretching of the carboxylic group upon labelling with ^{18}O was observed. These experimental findings confirmed the incorporation of ^{18}O-isotope into the carboxylic group during the catalytic process, validating the oxide relay functionality of the pendant carboxylic group during catalysis in complex **7**. Under acidic conditions, the basicity of the pendant carboxylic group is reduced largely. Therefore, the observed higher catalytic rate of **7** than **6** at pH 1 is certainly not due to the function of $-CO_2H$ in intramolecular proton-relay with the incoming water, which was proposed before under neutral to basic conditions for Ru-tda type complexes. The $-CO_2H$ group, close to the reactive formal $Ru^V{=}O$ unit, participated promptly in the intramolecular O–O bond formation reaction and promoted the water oxidation *via* the oxide relay pathway (Fig. 12). Mulliken spin density calculation of the formal $Ru^V{=}O$ species derived from **7** featured the electronic structure as "cationic-radicaloid-benzimidazole-Ru(III)-oxyl" species, thanks to the benzimidazole moiety for its redox-non-innocent character. The oxyl species being highly reactive most likely provoked the cleavage of the O–H bond of $-CO_2H$ and promoted the O–O bond formation *via* the radical coupling pathway (Fig. 12), presumably enabling the oxide relay function of the pendant carboxylic group even under highly acidic conditions. However, more detailed computational studies are required to get deeper insights into the mechanistic aspects, especially the O–O bond formation step.

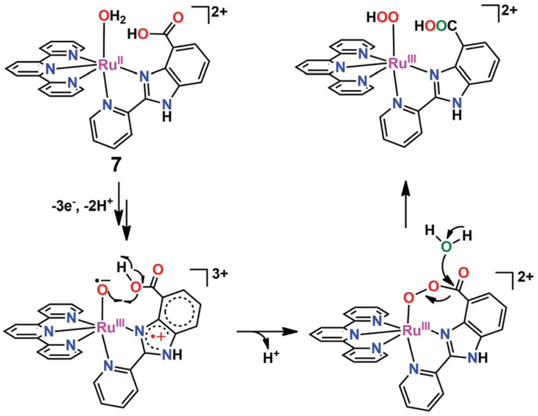

Fig. 12 Proposed O–O bond formation and oxide relay function of the dangling carboxylic group in the water oxidation reaction catalysed by complex **7** (ref. 18).

4.3. Phosphonate

In recent years the secondary coordination effect of the phosphonate group has also been studied. Llobet *et al.* extended their study with further modification of the tda ligand, where the two carboxylate groups were substituted by phosphonate groups leading to the 2,2′:6′,2″-terpyridine-6,6″-diphosphonate (tPa) ligand. With this ligand, a new Ru complex **8** was developed (Fig. 13).[27] In complex **8** the phosphonate group, owing to a pseudo-T_d geometry, would induce more structural distortions than that of the pseudo C_{2v} carboxylate group in Ru-tda complex. Moreover, the phosphonate group has stronger σ-donating property and more steric bulk than carboxylate. These would lead to different catalytic behaviour of **8** than that of the tda-analogue. Surprisingly, it appeared that complex **8** did not act as a true catalyst but as a pre-catalyst. The cyclic voltammogram of complex **8** at pH 7 did not show any electrocatalytic current due to water oxidation at a single anodic scan, implying complex **8** was apparently inactive towards water oxidation. Upon electrolysis at an applied potential of 1.30 V *vs.* NHE for 110 min at pH 7.7, complex **8** was quantitatively converted to complex **9**, where an oxygen atom was inserted between the Ru centre and one of the pyridyl groups of the tPa ligand (Fig. 13).[27] The X-ray structural analysis confirmed the formation of **9**. A computational analysis was performed to get insights into the transformation process from **8** → **9** (Fig. 14). At the applied potential, the initial six-coordinated Ru(II) complex **8** was oxidised and converted to a seven-coordinated Ru(IV) complex with two phosphonate groups bonded to the metal centre. At this oxidation state under basic conditions, an exogenous hydroxide ion bound to the Ru(IV) centre with the

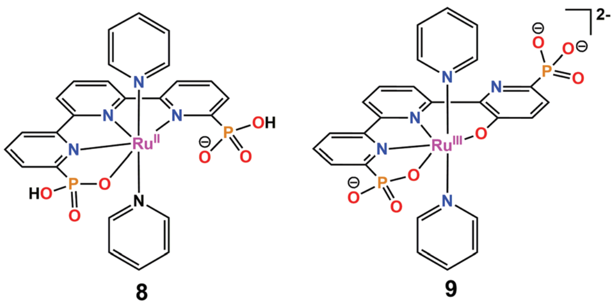

Fig. 13 Ru-Complexes with the dangling phosphonate group (ref. 27).

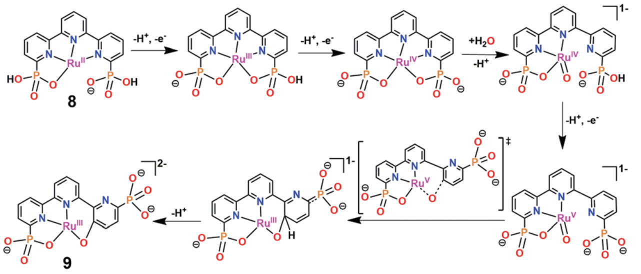

Fig. 14 Calculated reaction pathway of the formation of catalytically active species **9** from **8** under oxidative conditions at neutral pH (ref. 27). The axial pyridine ligands are not shown.

concomitant decoordination of one of the pyridyl phosphonate arms to produce a six-coordinated $[Ru^{IV}(O)(HtPa\text{-}\kappa\text{-}N^2O)(py)_2]^-$ species. This was further oxidised *via* PCET to generate reactive $[Ru^{V}(O)(tPa\text{-}\kappa\text{-}N^2O)(py)_2]^-$ to bring about the intramolecular aromatic CH bond hydroxylation to form species **9**. This ring hydroxylation process was energetically favoured from the thermodynamic perspective as obtained from the computation. Complex **9** turned out to be an excellent water oxidation catalyst achieving TOF_{max} values of 16 000 s^{-1} at neutral pH.

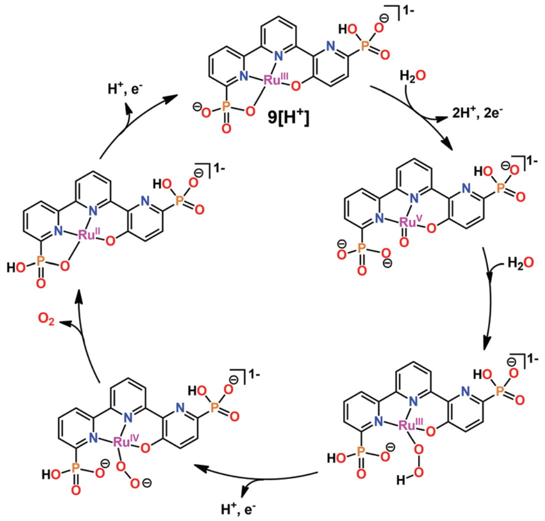

Fig. 15 Computed water oxidation pathway mediated by **9[H⁺]** at pH 7 (ref. 27). The axial pyridine ligands are not shown for clarity.

The catalytic pathway was proposed based on DFT calculations as shown in Fig. 15.[27] The active participation of the dangling phosphonate group in the intramolecular proton relay with the incoming water facilitated the rate-determining O–O bond formation *via* the WNA pathway. Notably, the alternative oxide relay pathway mediated by the pendant phosphonate group at neutral pH was energetically very unfavourable, unlike the event for the carboxylate group. Further investigations revealed that complex **9**, containing an easily oxidizable phenoxo group, suffered from oxidative degradation during the turnover condition and was converted to complex **10**, where a phosphonate and a carboxylate group bonded to the metal centre (Fig. 16).[28] Complex **10** was also a powerful WOC; however, it also suffered further transformations during electro-catalysis to various unknown active molecular water oxidation catalysts and ultimately degraded to RuO_2 nanoparticles along with a catalytically inactive species **11** (Fig. 16). Thus, the apparently-inactive complex **8** experienced a series of oxidative transformations to generate various molecular active intermediates, including RuO_2, and all contributed collectively to the catalytic performances. The pseudo-tetrahedral phosphonate group introduced a geometrical constraint in the complex structure that made the ligand susceptible to chemical transformations, leading to the degradation of the catalyst under oxidative conditions. On the other hand, the planar carboxylate derivative could enhance the stability of the catalyst as found in complex **3**. So, carboxylate might be a better choice than phosphonate for developing an oxidatively robust molecular WOC.

4.4. Pyridyl

Other than the anionic groups mentioned above, a pendant pyridyl group can also influence the reaction kinetics by controlling the secondary coordination sphere environment. Llobet and coworkers demonstrated this phenomenon using a mononuclear ruthenium(II) complex *trans*-$[Ru^{II}(L^{OMe}\text{-}\kappa\text{-}N^5)(Cl)]^{1+}$ (*trans*-**pre-12-Ru^II**) as the pre-catalyst, comprising of a rigid pentadentate ligand scaffold 6,6″-(methoxy(pyridin-2-yl)methylene)di-2,2′-bipyridine (L^{OMe}) (Fig. 17).[29] In aqueous pH 1/CF_3CH_2OH solution *trans*-**pre-12-Ru^II** experienced slow chloro-water exchange to generate a catalytically important aquo complex *trans*-$[Ru^{II}(L^{OMe}\text{-}\kappa\text{-}N^5)(H_2O)]^{2+}$ (*trans*-**12-Ru^II**). Upon treatment with one equivalent of Ce(IV) in 0.1 M

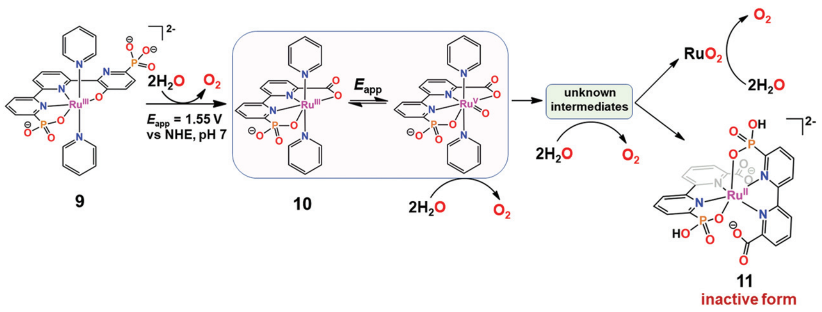

Fig. 16 Degradation of catalyst **9** to several intermediates during the water oxidation process at pH 7 (ref. 28).

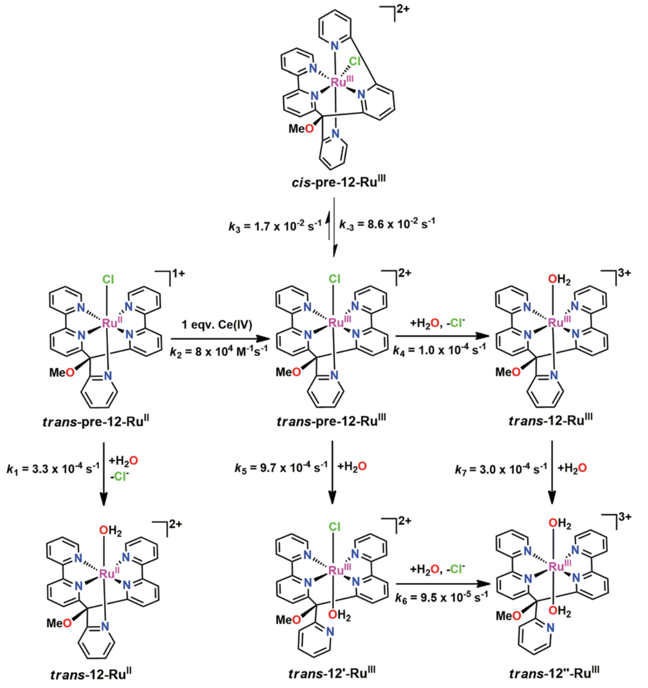

Fig. 17 Schematic representation of the formation of various substitution products derived from complex *trans*-**pre-12-Ru**^{II} (ref. 29).

CF_3SO_3H acid containing 5% CF_3CH_2OH, the Ru(II) complex *trans*-**pre-12-Ru**^{II} oxidised rapidly to form the corresponding Ru(III) complex *trans*-[Ru^{III}(L^{OMe}-κ-N^5)(Cl)]$^{2+}$ (*trans*-**pre-12-Ru**^{III}). It was observed that just after oxidation, complex *trans*-**pre-12-Ru**^{III} isomerized to its *cis*-form to a small extent and attained equilibrium very quickly, giving a *cis*–*trans* ratio of approximately 1 : 9. However, on keeping the solution for a longer time of about 15–50 minutes the *trans*-**pre-12-Ru**^{III} complex experienced a different degree of ligand substitution to generate a series of Ru–aquo species such as *trans*-[Ru^{III}(L^{OMe}-κ-N^5)(H$_2$O)]$^{3+}$ (*trans*-**12-Ru**^{III}), *trans*-[Ru^{III}(L^{OMe}-κ-N^4)(Cl)(H$_2$O)]$^{2+}$ (*trans*-**12′-Ru**^{III}) and *trans*-[Ru^{III}(L^{OMe}-κ-N^4) (H$_2$O)$_2$]$^{3+}$ (*trans*-**12″-Ru**^{III}) as shown in Fig. 17. At a prolonged time, the transient mono aquo species *trans*-**12-Ru**^{III} and *trans*-**12′-Ru**^{III} converted to the diaquo species *trans*-**12″-Ru**^{III}. The rate constants of various transformation/substitution reactions depicted in Fig. 17 were determined by mathematical fitting of kinetic data. Depending on the kinetic rate constants, the relative concentration of the transient species would vary over time. It was calculated that during the first 15–20 minutes after mixing Ce(IV) with *trans*-**pre-12-Ru**^{II} the chloro-aquo-Ru intermediate (*trans*-**12′-Ru**^{III}), having a dangling pyridyl group, formed predominantly in solution as compared to other species. Both the mono Ru^{III}–aquo species *viz trans*-**12-Ru**^{III} and *trans*-**12′-Ru**^{III} are potentially active catalysts, but the contribution from *trans*-**12-Ru**^{III} would be negligible, whereas the diaquo Ru^{III} species *trans*-**12″-Ru**^{III} was inactive towards water oxidation. The decoordination of the pyridyl group in complex *trans*-**12′-Ru**^{III} possessing this type of rigid ligand framework was favoured in accordance with DFT calculations, as it could release the strain on the structure. Complex *trans*-**12′-Ru**^{III} showed a promising water oxidation activity in a Ce^{IV}-driven reaction at pH 1, producing an initial TOF of 0.71 s^{-1} and a TON of 24 with a catalytic efficiency of 96% (with respect to 100 equivalents of Ce(IV)). On the other hand, complex *trans*-**12-Ru**^{II}, without a pendant base, produced only a modest TOF of 0.037 s^{-1} and a TON of 8 under the same conditions. In an electrochemical study, a larger electro-catalytic current was observed for complex *trans*-**12′-Ru**^{III} as compared to complex *trans*-**12-Ru**^{II}. Notably, the electro-catalytic wave of *trans*-**12′-Ru**^{III} was shifted by 200 mV cathodically with respect to that of *trans*-**12-Ru**^{II}. This cathodic shift was ascribed due to the stronger electron donation from the negatively charged chlorido ligand in *trans*-**12′-Ru**^{III}, which facilitated the generation of the catalytically active Ru^{V} oxidation state at a lower potential. Moreover, the dangling pyridyl group in *trans*-**12′-Ru**^{III} could also influence the outer coordination sphere interactions during the catalytic process. The transition state structure for the water nucleophilic attack at the Ru^{V}=O state of complex *trans*-**12′-Ru**^{III} was modelled successfully by adding an explicit solvent water molecule, as shown schematically in Fig. 18. Here it was found that the dangling pyridine formed a hydrogen bond with the incoming water and facilitated the O–O bond formation by accepting the proton. All these factors reduced the activation barrier for the rate-limiting water nucleophilic attack in complex *trans*-**12′-Ru**^{III} and subsequently enhanced the catalytic performances.

5. Secondary interactions between ancillary ligands

5.1. π–π interactions

Among the non-covalent interactions, π–π stacking interactions can induce the coupling of two metal–oxo/metal–oxyl units intermolecularly, which can substantially enhance the rate of the O–O bond-forming step. This strategy was found to be very promising in developing efficient molecular catalysts in the recent past. In this context, the water oxidation catalysts of type [Ru(bda)(X)$_2$] (bda = 2,2′-bipyridine-6,6′-dicarboxylate, X = N-heteroaromatic ring that occupied the axial positions) developed by Sun and coworkers are worth mentioning (Fig. 19).[30–32] The Ru-bda complexes catalysed water oxidation

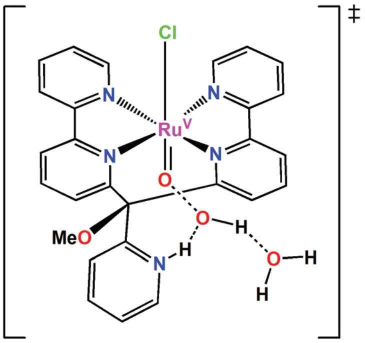

Fig. 18 Schematic representation of the transition state during the water nucleophilic attack at Ru^{V}=O species derived from *trans*-**12′-Ru**^{III} to form a "Ru^{III}–OOH" species (ref. 29).

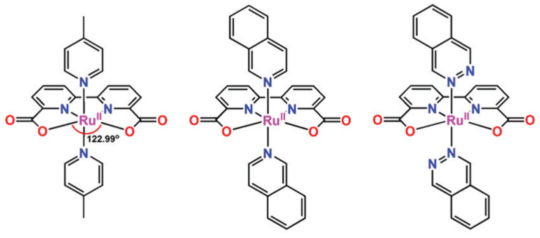

Fig. 19 Three representatives of the Ru-bda family of complexes.

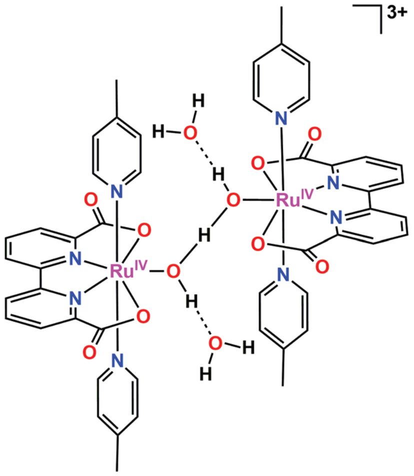

Fig. 20 Schematic view of the dimeric structure of Ru(IV)-complex $[Ru^{IV}(bda)(OH)(pic)_2]^+$ (ref. 30).

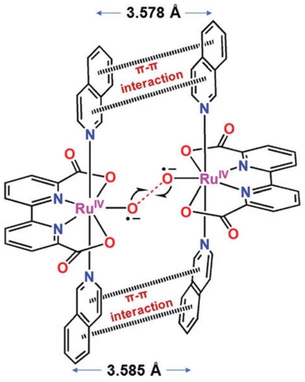

Fig. 21 Computed structure showing the non-covalent π–π stacking interactions between the isoquinolines, that facilitate the O–O bond formation *via* radical coupling of the two Ru^{IV}–oxyl units derived from complex **14** (ref. 31).

via the I2M pathway. The X-ray crystallography of complex $[Ru(bda)(pic)_2]$ (**13**) (pic = 4-picoline) revealed a unique structural feature.[30] It was found that the equatorial O–Ru–O bond angle (122.99°) deviated largely from the ideal 90° angle of an octahedral geometry. This large open-angle created a space for an extra ligation at the equatorial plane. In fact, a seven-coordinated 18e$^-$ Ru^{IV} species $[Ru^{IV}(bda)(OH)(pic)_2]^+$, having an extra equatorial hydroxide ligation, was structurally characterized, where two $[Ru^{IV}(bda)(OH)(pic)_2]^+$ units formed a dimer with a bridging $[HOHOH]^-$ unit (Fig. 20).[30] Two additional water molecules were H-bonded with $[HOHOH]^-$, providing extra stability. Moreover, these H-bonding networks might provide a proton relay channel during water oxidation. The discovery of this particular dimeric structure of the Ru(IV) intermediate established strongly the tendency of the two "Ru(bda)(OH)" molecular units to approach each other, which would facilitate the intermolecular O–O coupling between two active Ru^V═O (or Ru^{IV}–O$^•$) species. The kinetic study revealed a second-order dependence of the catalyst concentration on the reaction rate, validating the inter-catalyst coupling in the O–O bond formation step (I2M pathway). Complex **13** ([**13**] = 5.88 × 10^{-5} M) displayed a promising TON (2010 ± 57) and TOF (14.7 ± 3.4 s^{-1}) in a Ce^{IV}-driven reaction at pH 1.[31] At higher [**13**] (2.16 × 10^{-4} M), the TOF value significantly increased to 32.8 ± 3.1 s^{-1} since the rate of water oxidation followed a second-order kinetic dependence on the catalyst concentration. Later on, Sun's group replaced the two axial ligands (4-picoline) of complex **13** with two isoquinoline groups (**14**).[31] The isoquinoline groups in **14** showed stronger intermolecular π–π stacking interactions and less steric bulk as compared to 4-picoline in **13**, which facilitated the O–O coupling reaction significantly (Fig. 21).[31] This was manifested in achieving an impressive TON (8360 ± 91) and TOF (120.4 ± 8.2 s^{-1}) in a Ce(IV)-induced water oxidation reaction at a catalyst (**14**) concentration of 1.5 × 10^{-5} M. At higher [**14**] (2.16 × 10^{-4} M), the catalysis became very fast producing a TOF of 303 ± 9.6 s^{-1}, comparable to that of PS II.[31] In the Ru-bda series, the catalyst **15** with two axial phthalazine ligands exhibited the highest Ce^{IV}-driven water oxidation activity, displaying a huge TON of 55 419 ± 959 and TOF of 286 ± 21 s^{-1} at the catalyst concentration of 1.550 × 10^{-6} M and 2.222 × 10^{-4} M, respectively.[32]

5.2. Electrostatic interactions

Other than the π–π stacking, electrostatic interactions can also finely control the intermolecular O–O coupling process. The attractive force of electrostatic interaction can bring together two monomeric reactive units and direct them face to face for effective intermolecular coupling. In this context, spectacular work was done by Ahlquist and coworkers with Ru-bda complexes **16**, **17** and **18**, where the axial ligands contain charged groups (Fig. 22).[33] In complex **16**, the axial positions are occupied unsymmetrically by one positively and one negatively charged ligand. Complex **17** has both positively charged ligands and complex **18** has both negatively charged ligands at the axial positions. The Ce^{IV}-driven water oxidation activities of complexes **16–18** and the mixture of **17** and **18** in a 1 : 1 ratio (**M**) were investigated at pH 1. Complex **16** and mixture **M** showed significantly higher TOFs (12.4 s^{-1} for **16** and 34.4 s^{-1} for **M**) than those of **17**, **18** and $[Ru(bda)(pic)_2]$ (**13**) (TOF ∼ 1.54 s^{-1}) under [cat]/[Ce^{IV}] = 1 × 10^{-5} M/0.20 M condition.[33] The oxygen evolution kinetics for complex **16** followed the rate

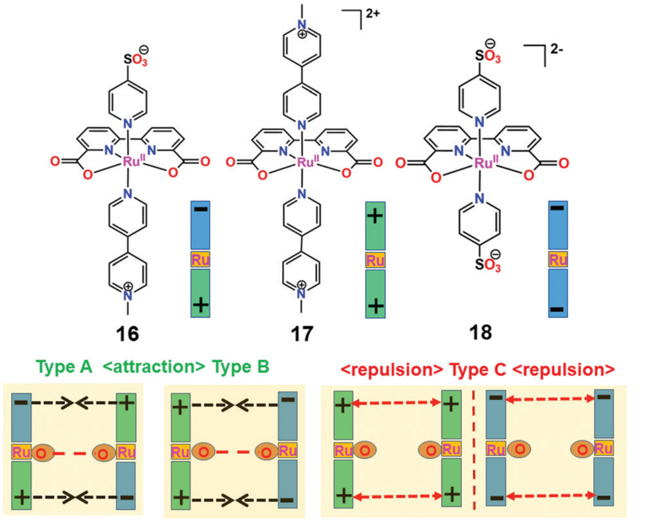

Fig. 22 (Top) The Ru-bda complexes with charged axial ligands, and (bottom) effect of electrostatic interactions in O–O bond formation (ref. 33).

law, rate = $k[\mathbf{16}]^2$. On the other hand for the mixture **M**, the rate equation obeyed the first-order dependence on the initial concentrations of both complexes **17** and **18** (rate = $k[\mathbf{17}][\mathbf{18}]$). These findings confirmed the I2M pathway, consistent with Sun's Ru-bda systems.[31] As reported, complexes **16–18** had very much comparable Ru^{III}/Ru^{II}, Ru^{IV}/Ru^{III}, and Ru^{V}/Ru^{IV} redox potentials, implying negligible impact of such axial groups on the electronic properties of the complexes. Therefore, the observed differences in catalytic performances are mostly due to the influence of electrostatic interactions exerted by the various charged axial ligands. In the case of catalyst **16**, two molecules can arrange themselves in an antiparallel manner (Type A) to form a stable ion pair. On the other hand for the mixture (**M**), the positively charged groups of complex **17** can make an ion pair with the negatively charged groups of complex **18** (Type B). Such self-assemblies of the Ru(II) complexes due to the attractive electrostatic interactions in type A and type B systems were identified by ^{1}H NMR, small-angle X-ray scattering (SAXS), cryotransmission electron microscopy (Cryo-TEM) and electrical conductivity experiments. The formations of type A and type B pre-reactive dimers due to attractive effects of positive–negative electrostatic interactions reduced the energy barrier for the dimerization of two $Ru^{V}{=}O$ units *via* the radical coupling pathway, enhancing the catalytic performances significantly for **16** and mixture **M**. In contrast, for complexes **17** and **18** the repulsive forces between two same charges dominated and precluded the dimer formation (Type C). As a consequence, the catalytic activities of discrete **17** and **18** were suppressed.

5.3. Hydrophobic–hydrophilic interactions

The hydrophobicity of axial pyridine ligands in Ru-bda type complexes can also influence the formation of the pre-organized dimer during the O–O coupling step (I2M pathway) between two $Ru^{V}{=}O$ units since the hydrophobic nature of the oxo group itself provides a significant driving force for dimerization.[34] The Sun group demonstrated the hydrophobic effects on water oxidation activity by designing complexes **19**, **20** and **21**, where the hydrophilic glycol chains at the *para*-positions of the axial pyridine groups were systematically substituted with hydrophobic alkyl chains (Fig. 23).[35] To study the hydrophobic effect exclusively, the axial ligand modifications in **19–20** were done judiciously so that the *para*-substituents did not create much electrostatic repulsions and steric hindrances, as well as avoiding π extensions. The crystal structure of **20,** as shown in Fig. 24, revealed strong CH–π interactions that might also play a vital role in pre-reactive dimer formation. The catalytic performances of **19–21** were evaluated in a Ce^{IV}-driven reaction at pH 1 and compared. The hydrophobic complexes **20** and **21** performed better than the hydrophilic complex **19** (TOF, s^{-1} = 81 (**19**), 118 (**20**), 146 (**21**); condition: [cat] = 100 μM, $[Ce^{IV}]$ = 1.2 mmol, pH 1). ^{1}H NMR, electrochemistry and steric mapping indicated that the catalytic performance did not correlate with the electronic and steric effects of the axial ligands, implying those factors had negligible influence on the reactivity. Interestingly, the reactivity could be correlated with the hydrophobicity of the axial ligands in complexes **19–21**. Computational simulations showed that the binding free ener-

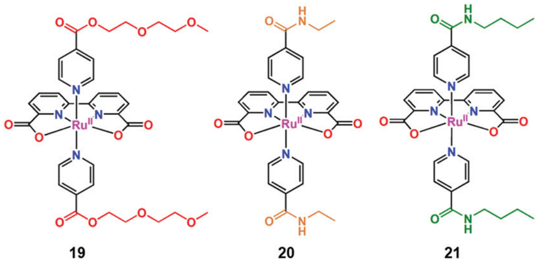

Fig. 23 Ru-bda complexes having variable hydrophobic axial ligands (ref. 35).

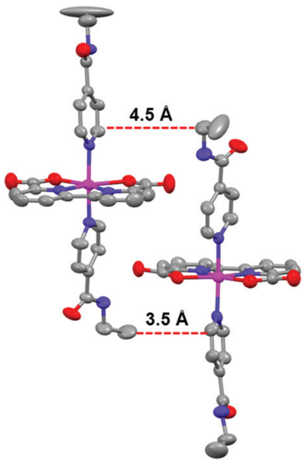

Fig. 24 The CH–π interactions found in the crystal structure of complex **20**. The structure has been regenerated from CCDC number 2091346 (ref. 35).

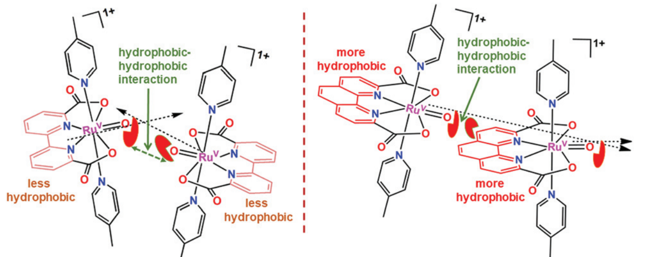

22 **23**

Fig. 25 Computationally simulated schematic representations of the (left) front-to-front, and (right) front-to-back orientation of the pre-reactive dimer of two $Ru^V{=}O$ species for complexes **22** and **23**, respectively (ref. 36).

gies of the formation of pre-reactive dimers became more negative (−3.46, −3.78, and −3.90 kcal mol^{-1} for complexes **19**, **20** and **21**, respectively) with the increase in the hydrophobicity of the ligand. Although the differences were minimal, these simulations supported that greater hydrophobicity on the axial ligands in Ru-bda type complexes could facilitate, to some extent, the formation of a stable pre-reactive dimer.

In another study with complexes $[Ru^V(bda)(O)(pic)_2]^{1+}$ (**22**) and $[Ru^V(pda)(O)(pic)_2]^{1+}$ (**23**) (pda = 1,10-phenanthroline-2,9-dicarboxylate), Ahlquist *et al.* computationally simulated that the hydrophobic/hydrophilic directionality might affect the reaction pathway of the water oxidation reaction.[36] The molecular dynamic (MD) simulations predicted two distinct orientations of **22** and **23** at the pre-reactive dimerization stage, as shown in Fig. 25. In the case of bda, the hydrophobic oxo of one molecule pointed towards the oxo of another molecule, leading to a front-to-front geometry of the pre-reactive dimer that favoured the O–O coupling reaction *via* the I2M pathway. In contrast, for pda the hydrophobic oxo of one molecule was directed towards the more hydrophobic phenanthroline backbone of another molecule, giving rise to a front-to-back geometry of the pre-reactive dimer for the pda system, thereby disfavouring the I2M mechanism. This inappropriate orientation made the water-nucleophilic attack viable for the Ru-pda complex instead of the I2M pathway. The reaction rate for Ru-pda was determined to be unimolecular with respect to the catalyst concentration, justifying the WNA pathway. Therefore, the appropriate modifications in hydrophobic directions of the ligand backbone may alter the reaction pathway, as observed in the Ru-bda and Ru-pda systems.

6. Supramolecular ruthenium complexes: macrocyclic effect

The transportation of protons in liquid water occurs *via* diffusion through the hydrogen-bonded water molecules following the Grotthuss mechanism. So, the presence of a hydrogen-bonded water network near the active centre would facilitate the proton-relay and consequently boost the water oxidation activity. In this regard, the "macrocyclic approach" was found to be very promising for developing efficient catalysts. The macrocyclic cavity can accommodate a large number of hydrogen-bonded water molecules in the vicinity of the reactive sites, resulting in a decrease in the activation barrier for the abstraction of protons. The Würthner group developed a series of trinuclear supramolecular macrocycles by connecting Ru(bda) fragments with various bridging ligands.[37–40] One such example includes complex $[Ru(bda)bpb]_3$ (**24**) where three Ru(bda) units are connected through 1,4-bis(pyrid-3-yl) benzene (bpb) linkers (Fig. 26a).[37] Complex **24** showed remarkable catalytic performance under the Ce^{IV}/pH 1/59% CH_3CN condition achieving TOF > 100 s^{-1}. The complex also showed outstanding activity in a photo-driven reaction (pH 7.2) even at nM concentration producing TOF > 13.1 s^{-1}. Noticeably, the macrocyclic complex exhibited higher catalytic performance than the single unit $[Ru(bda)(pic)_2]$ (**13**) under the same conditions. Kinetics and ^{18}O-labelling experiments established that the macrocyclic complex **24** promoted water oxidation *via* the WNA pathway, unlike the event for the monomeric $[Ru(bda)(pic)_2]$ complex that followed the I2M pathway. The steric hindrances, as well as the rigidity of the macrocycle, prevented the O–O bond formation *via* the intermolecular coupling pathway. Computational modelling of the $[Ru(bda)bpb]_3$ macrocycle with three Ru^{IV}-OH units and cavity-embedded water molecules estimated that up to ten hydrogen-bonded water molecules could be preorganized inside the supramolecular cavity of complex $[Ru^{IV}\text{-}OH(bda)bpb]_3{}^{3+}$ (Fig. 26b). The X-ray structural analysis of the fluoro-derivative of the trinuclear Ru macrocycles at the Ru(II) state revealed the presence of indeed trapped hydrogen-bonded water molecules inside the hydrophobic cavity.[40] Such an extensive hydrogen-bonded network inside the cavity reduced the activation barrier for the water nucleophilic attack by activating the water molecule to such an extent that the rate-limiting step was switched from the water nucleophilic attack at the "$Ru^V{=}O$" state to the PCET oxidation from "Ru^{IV}–OH" to "$Ru^V{=}O$". The hydrogen-bonded network acted as an exit channel for the protons involved in PCET processes, thereby accelerating the reaction kinetics significantly. In addition to that, the supramolecular architecture also provided higher stability to the catalyst due to

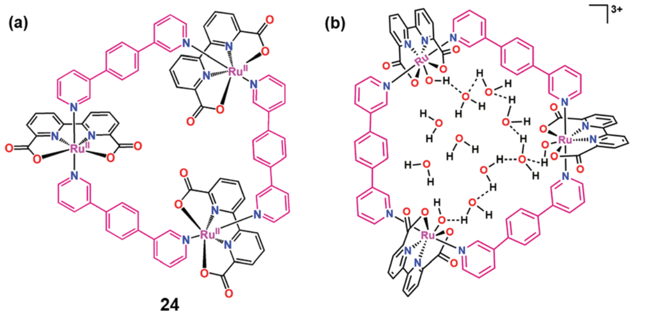

24

Fig. 26 Schematic drawings of (a) the structure of trinuclear macrocyclic compound $[Ru(bda)bpb]_3$ (**24**) and, (b) the DFT optimized structure of $[Ru^{IV}\text{-}OH(bda)bpb]_3{}^{3+}$ with cavity-embedded water molecules (ref. 37).

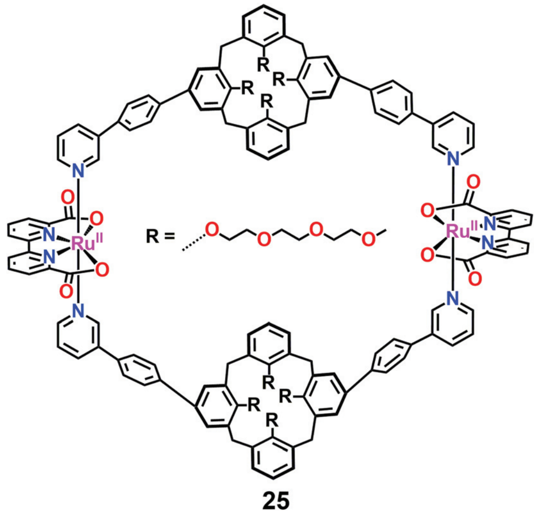

25

Fig. 27 Drawing of the dinuclear macrocyclic compound **25** (ref. 41).

the chelate effect. If somehow one of the pyridyl moieties of the bridging ligand decoordinates from one of the metal centres, then there is a high probability that it may rebound to the metal centre as the other end is still attached to another metal centre. Such a self-healing process enabled the macrocyclic complex to maintain its molecular integrity for a long time even under drastic oxidising conditions.

In another report, the Würthner group described a calix[4]arene-based cyclic dinuclear Ru-complex (**25**) for the homogeneous catalytic water oxidation reaction (Fig. 27).[41] Similar to **24**, complex **25** also showed increased catalytic activity compared to mononuclear [Ru(bda)(pic)$_2$] (**13**) under the same experimental conditions. Kinetic studies, including the determination of kinetic isotope effects (k_{H2O} = 4.2 s^{-1}, k_{D2O} = 2.4 s^{-1}; 40% CH_3CN/pH 1 triflic acid, Ce(IV) as the oxidant; primary KIE ~ 1.8), established a WNA mechanism with the involvement of a secondary coordination sphere. Complex **25** produced an average TOF of 19 s^{-1} in a chemically driven water oxidation reaction. It also displayed an outstanding TOF of 15.5 s^{-1} in a photo-driven reaction even under highly diluted conditions (nM concentration) in pH 7 aqueous medium containing 40% CH_3CN as co-solvent.

With the inspiration of the fact that the cyclic compounds can preorganize the substrate water molecules and boost the catalytic rate, Sun *et al.* in their recent publication reported four monomeric Ru-bda cyclic compounds **26–29**, where the ring size and the hydrophilic/hydrophobic microenvironments exerted by the distal ligands were systematically varied (Fig. 28).[42] As observed for the non-cyclic compounds (**19–21**), here also for the cyclic compounds, the hydrophobic environment on the outer sphere exerted a promotional effect on catalytic performances. The cyclic compounds with a hydrophobic environment performed better than their hydrophilic analogues in a Ce^{IV}-driven water oxidation reaction at pH 1 with TOF (s^{-1}) values 1.3 (**26**), 2.3 (**27**), 5.7 (**28**), and 34.1 (**29**). From the ^{1}H NMR studies, it could be envisaged that in the case of complexes **26**, **27** and **29** the distal ligands preferred a locked conformation, restricting the switch over from left to right in front of the catalytic site. On the other hand, for complex **28**, the large hydrophilic distal ligand showed more rotational flexibility. The structural analyses of **26** and **28** (Fig. 29) showed that the distal ligand in each complex deviated from the vertical axis of the active site, giving rise to an offset angle of 22.8° for **26** and 37.3° for **28**. The higher deviation in the case of **28** than **26** implies that the larger hydrophilic ligand has relatively higher rotational flexibility than its smaller counterpart. Therefore, the occurrence of distal ligands with locked-conformation in front of the catalytic sites in complexes **26**, **27** and **29** hindered the I2M pathway and made the WNA pathway more competitive. In contrast, for **28**, having more rotational flexibility, both the pathways I2M and WNA became operational. The distal ligands in complexes **26–29** also influenced the surrounding water network that could be finely

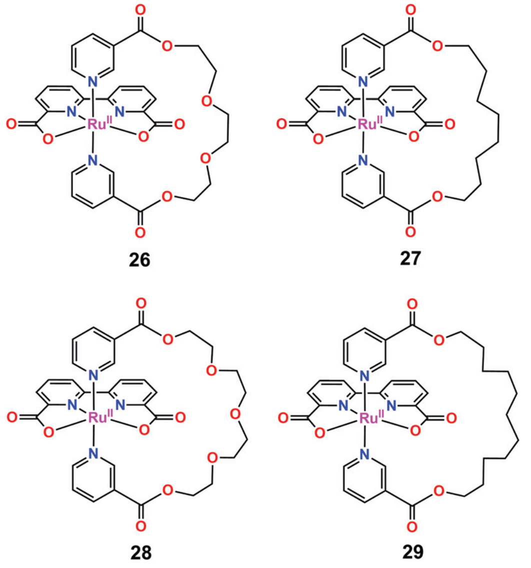

Fig. 28 Monomeric cyclic Ru-complexes with a variable hydrophilic–hydrophobic microenvironment (ref. 42).

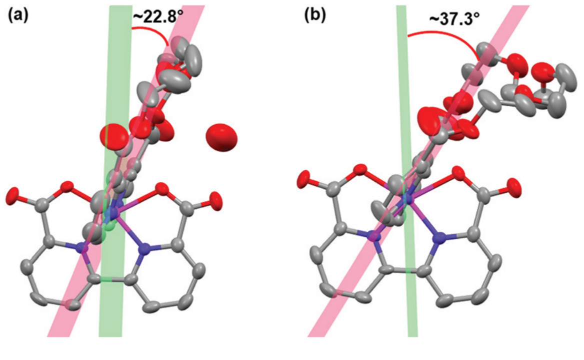

Fig. 29 X-ray crystal structures (top view) of complex (a) **26·H$_2$O** and (b) **28·H$_2$O** showing the deviation of the cyclic ring from the vertical axis of the active site. The crystal structures in (a) and (b) have been regenerated from the CCDC numbers 1955358 (ref. 43) and 2056826, respectively (ref. 42).

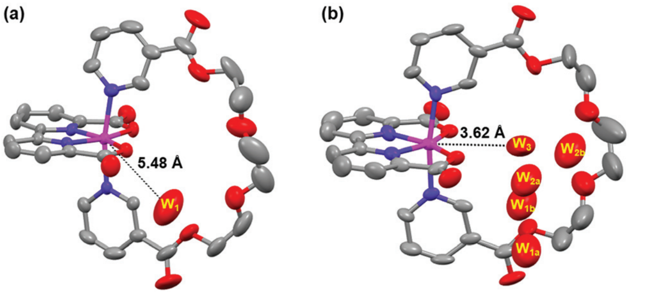

Fig. 30 X-ray crystal structures (side view) of (a) Ru(II) complex **26·H₂O** and (b) Ru(III) complex $\mathbf{26^+ \cdot 3H_2O \cdot CH_3CN \cdot PF_6^-}$. Except for water other solvent molecules and the counter anion are omitted for the Ru(III) complex. The crystal structures in (a) and (b) have been regenerated from the CCDC numbers 1955358 and 1986038, respectively (ref. 43).

tuned by the hydrophobicity/hydrophilicity of the pocket ligands. In the crystal lattice of Ru(II)-complex **26**, a single water molecule was present between the ether linkages of the macrocyclic ligand and the bda-carboxyl group.[42,43] However, this water molecule was not well-directed towards the catalytic site, residing 5.48 Å far apart from the Ru(II) centre and deviating largely from the equatorial bda plane (Fig. 30a). Interestingly, three preorganized water molecules were found in the crystal lattice of **26** at the Ru(III) state ($\mathbf{26^+}$).[43] Out of them, one water molecule pointed towards the seventh coordination zone of the metal centre at the equatorial plane with a $Ru^{III} \cdots OH_2$ distance of 3.62 Å only (Fig. 30b). Therefore, the structural characterisations of **26** at the Ru^{II} and Ru^{III} oxidation states provide valuable informations regarding how the substrate water molecules are being organized and get ready for the reaction with the active site. A calculated model of **27** at the Ru^{III} state incorporating three solvent water molecules ($\mathbf{27^+ \cdot 3H_2O}$) was established by DFT calculations, and it was compared with the optimized structure of the Ru(III) complex $\mathbf{26^+ \cdot 3H_2O}$ to reveal the effect of hydrophobicity on the preorganization of water molecules.[42] Notably, on changing the microenvironments from hydrophilic to hydrophobic, the distances between Ru^{III} and the nearby water were altered from the non-bonding mode (for hydrophilic catalyst $\mathbf{26^+}$) to the bonding mode (for hydrophobic catalyst $\mathbf{27^+}$) with a decrease of the $Ru^{III} \cdots OH_2$ distance from 3.53 Å to 2.66 Å in the gas phase and from 3.62 Å to 2.83 Å considering the solvation model. These results indicated that the hydrophobic distal ligand in **27** repelled the water molecules and pushed them towards the active centre. A similar situation might also prevail to a greater extent in complex **29** with a larger hydrophobic pocket, showing significantly higher activity with a TOF value of 34.1 s^{-1} *via* the WNA pathway.

7. Secondary interactions to anchor molecular catalysts on a solid surface

Immobilization of the molecular WOCs onto a solid conducting surface is the next step in engineering to develop a heterogeneous (photo)electro-anode that may be used to fabricate a water-splitting device. On this account, it is imperative to select a molecular catalyst that promotes water oxidation *via* the WNA pathway, as it can function even under restricted mobility conditions. The conventional anchoring moieties such as carboxylate or phosphonate have inadequate stability in water, especially in the presence of supporting electrolytes.[44,45] In a recent development, secondary interactions such as π–π stacking and C–H···π interactions have been successfully used to anchor molecular catalysts on solid conducting surfaces such as multi-walled-carbon-nanotubes (MWCNTs). The Ru-tda type complexes that showed remarkable performances in homogeneous conditions were heterogenized on the surface of MWCNTs by functionalizing the axial pyridyl type ligands with the pyrenyl group. The pyrene group in complexes **30** and **31** (Fig. 31) allowed effective anchoring of the Ru-tda units on the surface of MWCNTs *via* extensive π-interactions without significant modification of the inherent electronic and geometric properties of the parent complex.[45,46] These hybrid materials were found to act as a robust electro-

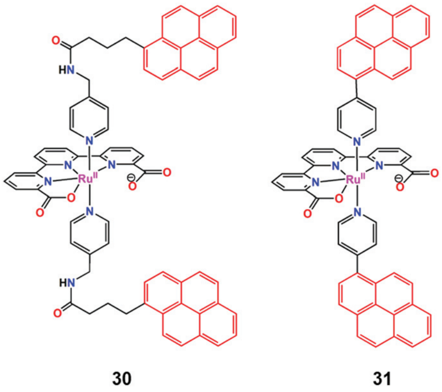

Fig. 31 Ru-tda family of complexes having the pyrenyl group attached on the axial ligand framework (ref. 45).

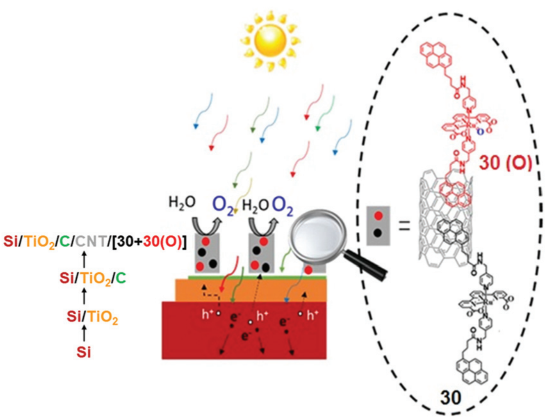

Fig. 32 Schematic representation of the photoanode *n*-Si/TiO₂/C/MWCNT/**30**. Adapted with permission from ref. 46. Copyright 2017 American Chemical Society.

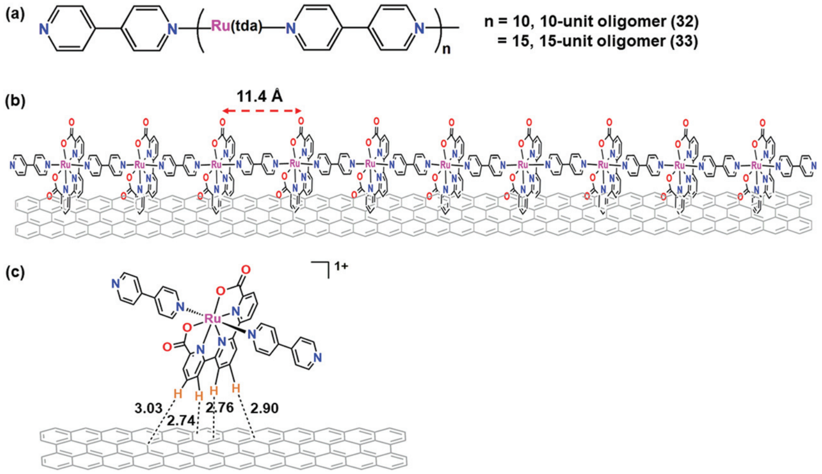

Fig. 33 Schematic representations of: (a) 10-unit and 15-unit oligomers of the Ru(tda) complex; (b) DFT optimized structure of the 10-unit-oligomer anchored on a graphene surface; (c) C–H⋯π interactions of one of the Ru fragments of the 10-unit-oligomer with the graphene surface (ref. 47).

anode for water oxidation producing approximately a million turnovers at pH 7 at an applied potential of 1.45 V *vs.* NHE without much degradation.[45] The immobilised **30** onto CNTs (**MWCNT**/**30**) had been drop-cast on Si electrodes coated with amorphous TiO_2 and sputtered C, generating material *n*-Si/TiO_2/C/MWCNT/**30** that functioned as a promising photoanode for the water oxidation reaction at neutral pH (Fig. 32).[46]

In a recent report, Llobet *et al.* introduced for the first time another simple method, C–H⋯π interactions, to immobilize molecular catalysts onto MWCNTs. The various chain length coordination oligomers of Ru-tda using 4,4′-bypiridine as the bridging ligand were synthesized and successfully anchored on a graphite surface (Fig. 33a).[47] XAS analysis revealed that upon anchoring onto the MWCNT surface under aerobic conditions, almost 96% of Ru(II) in oligomeric compounds got oxidised to the Ru(III) state. The drawing of the DFT/MM-optimized structure of a 10-unit oligomer, $[Ru(tda)(4,4'\text{-}bpy)]_{10}(4,4'\text{-}bpy)$ (**32**) anchored on a graphite surface is shown in Fig. 33b. Here the binding occurred *via* C–H⋯π interactions between the CH bonds of the auxiliary ligand of the Ru complex and the π-rings of the graphite surfaces. Four CH bonds per monomeric unit (two from the central pyridyl and the other two from one of the terminal pyridyl rings of tda ligand) interacted with the surface as shown in Fig. 33c. Here thermodynamics played a vital role in effectively anchoring the oligomers onto the surface. The computed Gibbs free energy of binding ($\Delta G°$) of the 10-unit oligomer was obtained as −133 kcal mol^{-1}, where the contribution from the binding enthalpy ($\Delta H°$) and the entropic penalty ($T\Delta S°$) was −150 kcal mol^{-1} and −17 kcal mol^{-1}, respectively. Therefore, each Ru-tda unit contributed roughly a value of −15 kcal mol^{-1} binding enthalpy for attaching to the surface. On the other hand, the entropic change deals with the association between the catalyst and the surface. During adsorption on the surface, the net changes in the number of components will not differ much from monomer to oligomer. Consequently, the entropic penalty will have a negligible dependence on the size of the oligomer. Therefore, for a monomeric complex to bind with the surface, the interaction Gibbs free energy would be (−15 + 17) kcal mol^{-1} = +2 kcal mol^{-1}. The positive Gibbs free energy implied a non-bonding interaction of a monomer complex to the solid surface. However, if the monomeric complexes are threaded to make a polymer, each small C–H⋯π binding interaction can collectively contribute to the overall binding enthalpy, which would increase with the increase of the length of the polymer. Thus, many small binding interactions can make the interaction Gibbs free energy negative for favourable and effective adsorption on the graphite surface. Indeed, a very effective hybrid material with a 15-unit oligomer (**33**) anchored on CNT was developed, and this material could produce a remarkable current density of 32 mA cm^{-2} at pH 7 in a bulk electrolysis experiment for 12 hours at an applied potential of 1.86 V *vs.* RHE, generating overall TONs of ~2×10^5 with faradaic efficiencies above 99%.[47]

8. Conclusions and outlook

Water-splitting has paved a new avenue for the sustainable energy economy. Water oxidation is the foremost hurdle to building a hydrogen-based energy economy from the water-splitting reaction. Over the past years, the field of water oxidation catalysis has experienced exponential advancement with the development of numerous WOCs. However, the required TON and TOF values for large-scale application are yet to be achieved. The proper design of ligands is of fundamental importance in developing efficient and long-lasting molecular catalysts. In this article, we reviewed the effects of the secondary coordination sphere in the water oxidation reaction catalysed by a few selected Ru-complexes. The outer sphere interactions positively impacted catalytic performances, particularly in boosting the reaction rate. A dangling base such as sulfonate, carboxylate, phosphonate, pyridyl group, *etc.* could facilitate the proton relay and stabilize the intermediates by providing a hydrogen-bonding site. Even a suitably placed carboxyl group in the outer coordination sphere could enhance the catalytic rate by participating in the O–O bond-forming step and promoting the reaction *via* the oxide relay pathway. The π–π stacking, electrostatic interaction, hydrophobic environment, *etc.* also could fine-tune the O–O bond formation step. The macrocyclic cavity could accommodate a hydrogen-bonded water network that facilitated the proton transfer processes. All these fine tunings on the secondary sphere played a vital role in decreasing the energy barrier of the rate-determining step and ensured fast catalysis. Remarkable TOF values, comparable to or even higher than that of the natural photosystem II, have been achieved employing the secondary interactions in the design principle of molecular catalysts. Furthermore, secondary interactions such as π–π and CH⋯π interactions could be used simply to immobilize molecular catalysts effectively onto solid conducting surfaces such as carbon nanotubes to develop photo(electro)-anodes. In a nutshell, the design of catalysts interplaying with outer-sphere coordination has now rewarded the scientific community with some state-of-the-art WOCs.

Despite the considerable improvement, especially in achieving a very high TOF, the stability of the molecular catalyst under strongly oxidising conditions is still a major concern for useful application. In this context, developing methodologies that can repair the catalyst by self-healing is essential for long-lasting catalysis. A rigid and oxidatively robust ligand framework can assist in preserving the molecular integrity of the catalyst under harsh conditions. The macrocycle approach is promising as it can prevent the ligand decoordination *via* the chelate effect. Further investigations should be directed to develop WOCs based on the first-row transition metal ions due to the insufficiency of the ruthenium metal. However, the intrinsic labilities of the first-row metal ions, in general, make it difficult for the first-row complexes to behave as robust molecular WOCs.[48] The lessons learnt with the Ru-complexes interplaying with the secondary interactions may also be employed to develop first-row WOCs. We believe that further exploration of the secondary coordination sphere might pave the way for producing economically viable, efficient WOCs to meet the standards for practical applications.

Author contributions

AG and SD performed the literature survey and prepared a small summary of all relevant papers. AK contributed to the oxide relay work published by SM's group. AG prepared the initial draft; SM revised it and wrote the final version.

Conflicts of interest

There are no conflicts to declare.

Acknowledgements

Financial support from the Council of Scientific and Industrial Research, Government of India [Grant 01(3052)/21/EMR-II to SM] is gratefully acknowledged. SM thanks all his co-authors/collaborators whose names appear in the appropriate literature citations. AG, SD and AK sincerely thank IIT Kharagpur for the award of the institute Ph.D. fellowship.

Notes and references

1 H. Ritchie and M. Roser, *Energy—Our World in Data*, 2020.

2 Paris agreement, 2015, log on from: **https://unfccc.int/files/essential_background/convention/application/pdf/english_paris_agreement.pdf**.

3 M. Gul, Y. Kotak and T. Muneer, *Energy Explor. Exploit.*, 2016, **34**, 485–526.

4 J. M. Berg, J. L. Tymoczko, G. J. Gatto, Jr. and L. Stryer, *Biochemistry*, W. H. Freeman & Company, 8th edn, 2015.

5 The efficiency of photosynthesis is calculated as described in reference no. 4. The change in Gibbs free energy ($\Delta G°$) for the reduction of CO_2 to glucose is 477 kJ mol^{-1}. The reduction of one mol of CO_2 to glucose is a four-electron process. Hence, two equivalents of NADPH are required to accomplish this reduction in PS I. The reducing equivalents needed for PS I are generated from the water oxidation at PS II by absorbing photons with wavelengths lesser than 680 nm. In overall photosynthesis, eight photons are needed to create one O_2, two NADPH and three ATP molecules. The energy content of one mol of a photon of wavelength 600 nm is 199 kJ. Therefore, eight moles of such photons correspond to 1592 kJ of energy. So, the nominal efficiency of photosynthesis at standard conditions is $(477/1592) \times 100 = 30\%$.

6 M. D. Karkas, O. Verho, E. V. Johnston and B. Akermark, *Chem. Rev.*, 2014, **114**, 11863–12001.

7 D. R. Ort and C. F. Yocum, *Oxygenic Photosynthesis: The Light Reactions*, Kluwer Academic Publishers, 2004.

8 Y. Umena, K. Kawakami, J. R. Shen and N. Kamiya, *Nature*, 2011, **473**, 55–60.

9 M. Suga, F. Akita, K. Hirata, G. Ueno, H. Murakami, Y. Nakajima, T. Shimizu, K. Yamashita, M. Yamamoto, H. Ago and J.-R. Shen, *Nature*, 2015, **517**, 99–103.

10 I. D. Young, M. Ibrahim, R. Chatterjee, S. Gul, F. D. Fuller, S. Koroidov, A. S. Brewster, R. Tran, R. Alonso-Mori, T. Kroll, T. Michels-Clark, H. Laksmono, R. G. Sierra, C. A. Stan, R. Hussein, M. Zhang, L. Douthit, M. Kubin, C. de Lichtenberg, L. Vo Pham, H. Nilsson, M. H. Cheah, D. Shevela, C. Saracini, M. A. Bean, I. Seuffert, D. Sokaras, T.-C. Weng, E. Pastor, C. Weninger, T. Fransson, L. Lassalle, P. Bräuer, P. Aller, P. T. Docker, B. Andi, A. M. Orville, J. M. Glownia, S. Nelson, M. Sikorski, D. Zhu, M. S. Hunter, T. J. Lane, A. Aquila, J. E. Koglin, J. Robinson, M. Liang, S. Boutet, A. Y. Lyubimov, M. Uervirojnangkoorn, N. W. Moriarty, D. Liebschner,

P. V. Afonine, D. G. Waterman, G. Evans, P. Wernet, H. Dobbek, W. I. Weis, A. T. Brunger, P. H. Zwart, P. D. Adams, A. Zouni, J. Messinger, U. Bergmann, N. K. Sauter, J. Kern, V. K. Yachandra and J. Yano, *Nature*, 2016, **540**, 453–457.

11 F. Allgower, A. P. Gamiz-Hernandez, A. W. Rutherford and V. R. I. Kaila, *J. Am. Chem. Soc.*, 2022, **144**, 7171–7180.

12 L. Tong and R. P. Thummel, *Chem. Sci.*, 2016, **7**, 6591–6603.

13 A. Kundu, S. Khan, S. Dey, C. Dutta, A. Anoop and S. Mandal, *Eur. J. Inorg. Chem.*, 2019, 164–177.

14 D. W. Shaffer, Y. Xie and J. J. Concepcion, *Chem. Soc. Rev.*, 2017, **46**, 6170–6193.

15 M. Yoshida, S. Masaoka, J. Abe and K. Sakai, *Chem. – Asian J.*, 2010, **5**, 2369–2378.

16 A. Kundu, S. K. Dey, S. Dey, A. Anoop and S. Mandal, *Inorg. Chem.*, 2020, **59**, 1461–1470.

17 S. Zhan, J. A. De Gracia Trivino and M. S. G. Ahlquist, *J. Am. Chem. Soc.*, 2019, **141**, 10247–10252.

18 A. Kundu, S. K. Barman and S. Mandal, *Inorg. Chem.*, 2022, **61**, 1426–1437.

19 M. Zhao, H.-B. Wang, L.-N. Ji and Z.-W. Mao, *Chem. Soc. Rev.*, 2013, **42**, 8360–8375.

20 A. G. Nash, C. J. Breyer, B. D. Vincenzini, G. I. Elliott, J. Niklas, O. G. Poluektov, A. L. Rheingold, D. K. Smith, D. G. Musaev and D. B. Grotjahn, *Angew. Chem., Int. Ed.*, 2021, **60**, 1540–1545.

21 H. N. Kagalwala, L. Tong, R. Zong, L. Kohler, M. S. G. Ahquist, T. Fan, K. J. Gagnon and R. P. Thummel, *ACS Catal.*, 2017, **7**, 2607–2615.

22 M. Yoshida, M. Kondo, S. Torii, K. Sakai and S. Masaoka, *Angew. Chem., Int. Ed.*, 2015, **54**, 7981–7984.

23 B. Das, A. Rahaman, A. Shatskiy, O. Verho, M. D. Kärkäs and B. Åkermark, *Acc. Chem. Res.*, 2021, **54**(17), 3326–3337.

24 R. Matheu, M. Z. Ertem, J. Benet-Buchholz, E. Coronado, V. S. Batista, X. Sala and A. Llobet, *J. Am. Chem. Soc.*, 2015, **137**, 10786–10795.

25 A. Shatskiy, A. A. Bardin, M. Oschmann, R. Matheu, J. Benet-Buchholz, L. Eriksson, M. D. Karkas, E. V. Johnston, C. Gimbert-Surinach, A. Llobet and B. Akermark, *ChemSusChem*, 2019, **12**, 2251–2262.

26 R. Matheu, M. Z. Ertem, M. Pipelier, J. Lebreton, D. Dubreuil, J. Benet-Buchholz, X. Sala, A. Tessier and A. Llobet, *ACS Catal.*, 2018, **8**, 2039–2048.

27 N. Vereshchuk, R. Matheu, J. Benet-Buchholz, M. Pipelier, J. Lebreton, D. Dubreuil, A. Tessier, C. Gimbert-Suriñach, M. Z. Ertem and A. Llobet, *J. Am. Chem. Soc.*, 2020, **142**, 5068–5077.

28 N. Vereshchuk, J. Holub, M. Gil-Sepulcre, J. Benet-Buchholz and A. Llobet, *ACS Catal.*, 2021, **11**, 5240–5247.

29 M. Gil-Sepulcre, M. Bçhler, M. Schilling, F. Bozoglian, C. Bachmann, D. Scherrer, T. Fox, B. Spingler, C. Gimbert-Surinach, R. Alberto, R. Bofill, X. Sala, S. Luber, C. J. Richmond and A. Llobet, *ChemSusChem*, 2017, **10**, 4517–4525.

30 L. Duan, A. Fischer, Y. Xu and L. Sun, *J. Am. Chem. Soc.*, 2009, **131**, 10397–10399.

31 L. Duan, F. Bozoglian, S. Mandal, B. Stewart, T. Privalov, A. Llobet and L. Sun, *Nat. Chem.*, 2012, **4**, 418–423.

32 L. Duan, C. M. Araujo, M. S. G. Ahlquist and L. Sun, *Proc. Natl. Acad. Sci. U. S. A.*, 2012, **109**, 15584–15588.

33 J. Yi, S. Zhan, L. Chen, Q. Tian, N. Wang, J. Li, W. Xu, B. Zhang and M. S. G. Ahlquist, *J. Am. Chem. Soc.*, 2021, **143**, 2484–2490.

34 S. Zhan, D. Martensson, M. Purg, S. C. L. Kamerlin and M. S. G. Ahlquist, *Angew. Chem., Int. Ed.*, 2017, **56**, 6962–6965.

35 T. Liu, G. Li, N. Shen, M. S. G. Ahlquist and L. Sun, *Energy Fuels*, 2021, **35**, 19096–19103.

36 S. Zhan, B. Zhang, L. Sun and M. S. G. Ahlquist, *ACS Catal.*, 2020, **10**, 13364–13370.

37 M. Schulze, V. Kunz, P. D. Frischmann and F. Würthner, *Nat. Chem.*, 2016, **8**, 576–583.

38 V. Kunz, J. O. Lindner, M. Schulze, M. I. S. Rohr, D. Schmidt, R. Mitrić and F. Wurthner, *Energy Environ. Sci.*, 2017, **10**, 2137–2153.

39 V. Kunz, M. Schulze, D. Schmidt and F. Würthner, *ACS Energy Lett.*, 2017, **2**, 288–293.

40 A.-L. Meza-Chincha, J. O. Lindner, D. Schindler, D. Schmidt, A.-M. Krause, M. I. S. Rohr, R. Mitrić and F. Wurthner, *Chem. Sci.*, 2020, **11**, 7654–7664.

41 N. Noll and F. Werthner, *Chem. – Eur. J.*, 2021, **27**, 444–450.

42 T. Liu, G. Li, N. Shen, L. Wang, B. J. J. Timmer, A. Kravchenko, S. Zhou, Y. Gao, Y. Yang, H. Yang, B. Xu, B. Zhang, M. S. G. Ahlquist and L. Sun, *Chem. – Eur. J.*, 2022, **28**, e202104562.

43 T. Liu, G. Li, N. Shen, L. Wang, B. J. J. Timmer, S. Zhou, B. Zhang, A. Kravchenko, B. Xu, M. S. G. Ahlquist and L. Sun, *CCS Chem.*, 2021, **3**, 2612–2621.

44 J. T. Hyde, K. Hanson, A. K. Vannucci, A. M. Lapides, L. Alibabaei, M. R. Norris, T. J. Meyer and D. P. Harrison, *ACS Appl. Mater. Interfaces*, 2015, **7**, 9554–9562.

45 J. Creus, R. Matheu, I. Penafiel, D. Moonshiram, P. Blondeau, J. Benet-Buchholz, J. Garcia-Antln, X. Sala, C. Godard and A. Llobet, *Angew. Chem., Int. Ed.*, 2016, **55**, 15382–15386.

46 R. Matheu, I. A. Moreno-Hernandez, X. Sala, H. B. Gray, B. S. Brunschwig, A. Llobet and N. S. Lewis, *J. Am. Chem. Soc.*, 2017, **139**, 11345–11348.

47 Md A. Hoque, M. Gil-Sepulcre, A. de Aguirre, J. A. A. W. Elemans, D. Moonshiram, R. Matheu, Y. Shi, J. Benet-Buchholz, X. Sala, M. Malfois, E. Solano, J. Lim, A. Garzón-Manjón, C. Scheu, M. Lanza, F. Maseras, C. Gimbert-Suriñach and A. Llobet, *Nat. Chem.*, 2020, **12**, 1060–1066.

48 M. Gil-Sepulcre and A. Llobet, *Nat. Catal.*, 2022, **5**, 79–82.